

Faraday Discussions

Accepted Manuscript



This is an Accepted Manuscript, which has been through the Royal Society of Chemistry peer review process and has been accepted for publication.

Accepted Manuscripts are published online shortly after acceptance, before technical editing, formatting and proof reading. Using this free service, authors can make their results available to the community, in citable form, before we publish the edited article. We will replace this Accepted Manuscript with the edited and formatted Advance Article as soon as it is available.

You can find more information about Accepted Manuscripts in the [Information for Authors](#).

Please note that technical editing may introduce minor changes to the text and/or graphics, which may alter content. The journal's standard [Terms & Conditions](#) and the [Ethical guidelines](#) still apply. In no event shall the Royal Society of Chemistry be held responsible for any errors or omissions in this Accepted Manuscript or any consequences arising from the use of any information it contains.

This article can be cited before page numbers have been issued, to do this please use: D. Katrantzi, S. Micklethwaite, N. S. Hondow, A. P. Brown and L. Dougan, *Faraday Discuss.*, 2024, DOI: 10.1039/D4FD00204K.

Unveiling the structure of protein-based hydrogels by overcoming cryo-SEM sample preparation challenges

Article Online
DOI: 10.1039/D4FD00204K

Dimitra Katrantzi¹, Stuart Micklethwaite¹, Nicole Hondow¹, Andy Brown¹, and Lorna Dougan²

¹ School of Chemical and Process Engineering, Faculty of Engineering and Physical Sciences, University of Leeds, UK

² School of Physics and Astronomy, Faculty of Engineering and Physical Sciences, University of Leeds, UK

Corresponding authors:

Lorna Dougan, L.Dougan@leeds.ac.uk

Dimitra Katrantzi, pmdka@leeds.ac.uk

Abstract

Protein-based hydrogels have gained significant attention for their potential use in applications such as drug delivery and tissue engineering. Their internal structure is complex, spans across multiple length scales and affects their functionality, yet is not well understood because of folded proteins sensitivity to physical and chemical perturbations and the high water content of hydrogels. Cryo-scanning electron microscopy (cryo-SEM) has the potential to reveal such hierarchical structure when hydrated hydrogels are prepared with appropriate cryofixation. We show for photochemically cross-linked, folded globular bovine serum albumin (BSA) protein hydrogels that preparation artefacts are reduced by in-situ gelation, high pressure freezing (HPF), plasma focused ion beam (pFIB) milling, sublimation, and low dose secondary electron imaging. Cryo-SEM of folded BSA protein hydrogels prepared in this way reveals a heterogeneous network with nanoscale porosity (~60 nm pores) surrounded by high secondary electron emission regions (~30 nm diameter) interconnected by narrower, lower emission regions (~20 nm length). This heterogeneous network structure is consistent with small angle scattering studies of folded protein hydrogels, with fractal-like clusters connected by intercluster regions. We further test the potential of cryo-SEM to detect the impact of protein unfolding on hydrogel network formation and reveal nanoscale differences in cluster sizes consistent with those derived from scattering data. Importantly, cryo-SEM directly images pores for sizing in both systems, with initial results on BSA suggesting protein unfolding induces an increase of ~10 nm in pore sizes. Our findings on cryo-SEM sample preparation challenges and solutions provide new opportunities to link hydrogel structure to function.

Introduction

Hydrogels are three-dimensional, hydrated, highly porous, percolating biopolymer networks spanning macroscopic dimensions. Hydrogels display rich viscoelastic properties, including mechanical strength and stress relaxation, and have hierarchical structures which span the nanoscale properties of the building blocks to the mesoscale of the cross-linked network structure.(1–3) The space within the hydrogel is critical to function, including the pore size between the cross-linked networks, since this can be exploited for a range of functions, including small molecule loading and release.(4–8) Morphological studies to accurately measure and understand the mesoscale structure of hydrogels are therefore important for exploiting hydrogels as biomaterials in applications such as medicine and healthcare.(8,9)

The most common techniques used to characterise the structure and morphology of supramolecular gels are scattering and microscopy.(10,11) Whilst both approaches offer valuable information on hydrogel properties, they each have well recognised challenges and limitations. As a result, an integrated approach is required to gain robust and meaningful insight into the structure of hydrogels.(12) Small angle scattering (SAS) techniques, including small angle X-ray scattering (SAXS) and small angle neutron scattering (SANS), are powerful tools for the *in-situ* bulk characterisation of



the gels, probing size, shape, internal structure and spatial arrangement on length scales between 0.25 and 300 nm, that require model fitting to extract real space information from the scattering of space.^(13,14) Microscopy techniques have the advantage of acquisition of real-space structures. However, they often require sample preparation, which can be prone to artefacts and only provide information about the local structure, requiring averaging to obtain a bulk overview.⁽¹⁵⁾

Recently, super-resolution microscopy has been employed for morphological studies of hydrogels providing measurements by automated approaches, but faced challenges such as biased image processing and lower resolution than electron microscopy (EM).⁽¹⁶⁾ There has been a long tradition of more than twenty years of using EM in an attempt to gain structural information on supramolecular gels.^(17–21) Scanning electron microscopy (SEM) is widely used for imaging the architecture of materials across different length scales due to its high resolution (typically 1-10 nm).^(22,23) SEM operates under high vacuum, which causes water evaporation and, therefore, requires drying of hydrated samples before imaging, which will cause structural alteration via shrinkage.^(24–27) Alternatively, cryo-SEM prohibits sample dehydration during imaging by examining a frozen sample at cryogenic temperatures.⁽²⁸⁾

Cryofixation is the most critical step for cryo-SEM, as an insufficient freezing rate results in ice crystal formation.⁽²⁹⁾ Ice crystals alter the sample structure because solutes are rejected to the boundaries of growing ice crystals, forming a segregation pattern determined by the cooling rate.^(30,31) By freezing at high cooling rates (i.e. very rapidly), water molecules are immobilised and remain in a non-crystalline state, resulting in a glass-like solid called vitreous (amorphous) ice.^(32,33) The cooling rate influences both nucleation and growth rates of crystalline ice, with slow cooling at ambient pressure, permitting formation of hexagonal ice, faster cooling producing cubic ice and only very rapid cooling inhibiting ice nucleation and vitrifying the water.⁽³³⁾ In an ideally cryo-immobilised sample, all water is vitrified, and solutes remain in their native/original environment.^(34,35) The commonly used bulk cryofixation methods are slush/liquid nitrogen freezing and high pressure freezing (HPF).

Freezing with liquid nitrogen consists of immersing a sample into a slush of liquid nitrogen (a mixture of solid and liquid) and is a widely used cryofixation method for hydrogels that results in the formation of a characteristic honeycomb-like gel structure.^(36–44) This technique, however, has a slow freezing rate (around 500 K/s) and is only ideal for samples with a thickness of less than 2-5 μm .^(30,45) HPF, on the other hand, has a larger thickness limit for the formation of vitreous ice because the sample is secured and frozen in liquid nitrogen under high pressure (2045 bar). Pressure lowers the crystalline ice nucleation temperature and inhibits expansion on crystallisation.⁽⁴⁶⁾ At ambient pressures, several 100000 K/s are required to vitrify a eukaryotic cell, whereas only a few 1000 K/s will be enough at 2045 bars.⁽⁴⁷⁾ The upper thickness limit for complete vitrification of a sample in HPF is 200-500 μm .^(47,48) HPF is now considered the cryofixation method to effectively cryoimmobilise cellular samples without morphological changes, and there are examples of wider application to other systems, including hydrogels.^(49,50) Given this and the developments in cryo-SEM, consideration should be given to their application to the full range of hydrogel materials, including emerging areas such as folded protein-based hydrogels.^(1,8,9)

In recent years, folded proteins have emerged as promising building blocks for constructing hydrogels. While studies have employed thermal or pH-induced denaturation of proteins to trigger gelation through physical cross-links^(51–54), there is a growing interest in retaining the fold of the protein to preserve its function in the hydrogel material. A pioneering study by Li *et al.* engineered a protein hydrogel aimed to mimic the mechanical properties of the giant muscle protein titin.⁽⁵⁵⁾ Further studies have engineered protein hydrogels mimicking the mechanical properties of tissues, forming highly elastic and stimuli-responsive materials, and dynamically regulating their properties and shape.^(37,56–66) Engineering of natural and synthetic proteins has enabled the formation of hydrogels with programmable properties.^(1,67,68) However, it remains challenging to understand how the nanoscale protein structure and mechanics translate to the macroscopic properties of the



hydrogel network. Given the sensitivity of proteins to physical and chemical perturbations, there is enormous potential in exploiting protein unfolding to modulate the dynamic properties of protein hydrogels. Indeed, it has become clear that protein unfolding is critical to network mechanics and the architecture of protein hydrogels.(69–71)

In particular, recent studies have highlighted the role of *in situ* unfolding and entanglement in defining hydrogel network mechanics.(70,72,73) For example, using bovine serum albumin (BSA) as a model protein, an integrated SANS and rheology analysis showed that *in situ* unfolding altered network topology and enhanced network mechanical rigidity.(70) More recently, protein unfolding has been exploited in a protein-polymer system that undergoes a unique strain stiffening and strengthening behaviour after shape recovery cycles.(71) Such control of *in situ* unfolding provides a powerful route for the design of tuneable biomaterials for medical and healthcare applications.(8,72) Given their potential, there is an urgent need to develop robust experimental methods to study the structure of protein hydrogels to determine and understand the impact of protein unfolding on the network structure and morphology. Here, we focus on the application of cryo-SEM for structural analyses of protein hydrogels.

For this purpose, the BSA protein was used as the building block to create protein-based hydrogels. BSA is a globular folded protein with attractive properties such as biodegradability, biocompatibility, low cost, non-immunogenicity, and drug binding capabilities, enhancing the properties of hydrogels when used as the building block.(74–76) The folded state of BSA is held together by 17 covalent disulphide bonds, which act as ‘nanostaples’ and stay intact during gelation (**Figure 1**). These mechanically robust covalent staples can withstand forces as high as 2 nN(77,78), far exceeding the 20-100 pN generated within the cross-linked protein network.(79) Moreover, these bonds can be removed by reducing agents such as dithiothreitol (DTT), making the protein force labile, allowing it to easily unfold under the forces generated during gelation. Together, these properties render BSA an ideal model for protein unfolding studies. For gelation, a photochemical crosslinking method is used, during which the solvent accessible surface tyrosine residues of BSA (**Figure 1**) crosslink with neighbouring BSA molecules by irreversible dityrosine bonding.(80) A schematic showing the photochemical crosslinking of a folded (mechanically robust) BSA to form a hydrogel is shown in **Figure 1**. Finally, we test this protocol on unfolded protein-based hydrogels composed of force labile BSA protein to detect morphological alterations to the gel network. Linking the cryo-SEM protocols and analysis methods we present to SAS models opens the possibility of complete structure-property evaluation of hydrogels in general.(70) The rheology of the final folded protein-based hydrogel is explored using a parallel plate geometry to confirm successful gelation. Previous SANS and SAXS studies have shown that the final BSA protein network consists of fractal-like clusters of proteins connected by intercluster regions of folded proteins (**Figure 1**). (2,70,73,81–83)



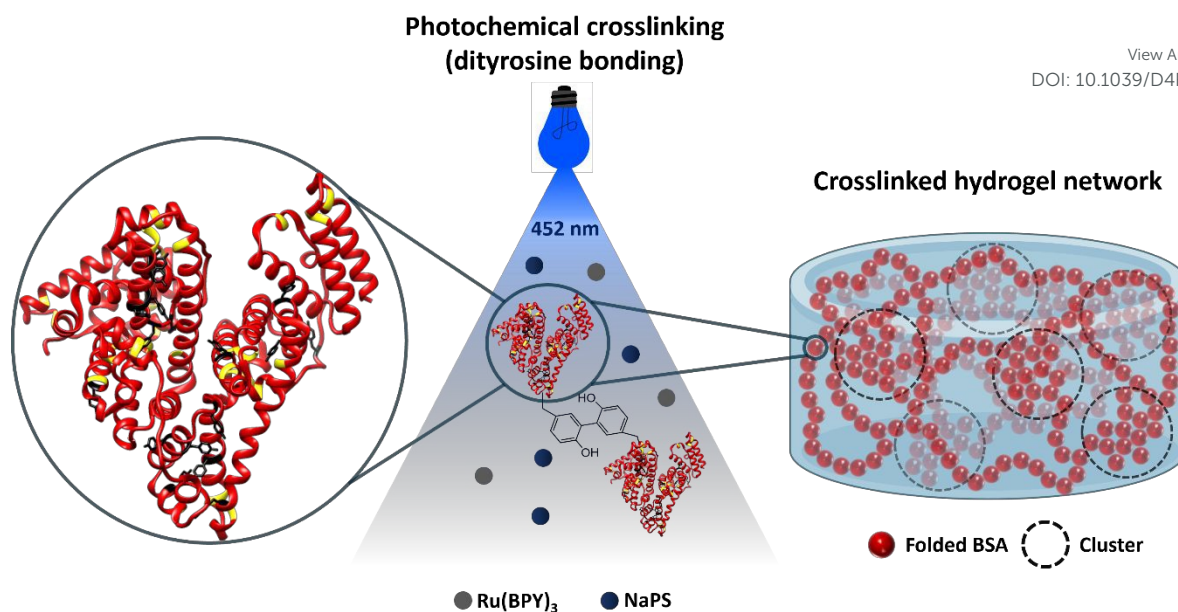


Figure 1. Schematic of folded BSA-based hydrogel synthesis by a Ru(BiPy)₃ catalysed photochemical crosslinking method (BSA PDB code: 3V03). Disulphide bonds are highlighted with yellow, and tyrosine residues with black. The mechanically robust disulphide bonds hold the folded state of BSA together and stay intact during gelation. The tyrosine residues are used for the crosslinking to form the hydrogel. In the presence of light, Ru(BiPy)₃ photo-oxidizes to Ru(BiPy)₃³⁺, and NaPS acts as an electron acceptor. The photoactivated Ru(BiPy)₃ extracts an electron from tyrosine, leading to tyrosine radical species that can covalently crosslink via dityrosine bonding, highlighted in the middle schematic, to form the hydrogel. The crosslinked hydrogel network schematic constructed by SAXS and SANS data(70) represents the BSA hydrogel network. The network consists of fractal-like clusters (dashed circles) made of folded proteins connected by more sparsely populated intercluster regions of folded proteins.

In this study, we develop a reproducible protocol for representative preparation and cryo-SEM imaging of folded protein-based hydrogels while identifying structural artefacts induced by ice crystallisation. We benchmark features of the vitrified gel network against those obtained by SAS analysis(2,70,73,81–83) and evaluate additional aspects of the morphology of these gels, such as pore sizes. Finally, we test this protocol on unfolded protein-based hydrogels composed of force labile BSA protein to detect morphological alterations to the gel network. Linking the cryo-SEM protocols and analysis methods we present to SAS models opens the possibility of complete structure-property evaluation of hydrogels in general.

Experimental

Materials

Bovine serum albumin (heat shock fraction, protease free and essentially globulin free), sodium persulfate (NaPS), tris(2,2'-bipyridyl)dichlororuthenium(II) hexahydrate (Ru(BiPy)₃), 1,4-dithiothreitol (DTT), sodium phosphate monobasic and sodium phosphate dibasic were purchased from Sigma-Aldrich and used without further treatment.

Hydrogel Preparation

As previously described(2,70,81,83), initially, a protein stock of 200 mg/mL BSA and a cross-link reagent stock of 100 mM NaPS and 200 μM Ru(BiPy)₃ are prepared. For the unfolded protein gels, 6 mM DTT is also prepared for the reagent stock. Hydrogel samples are prepared by mixing in a 1:1 mass



ratio of protein stock to cross-link reagent stock to obtain final concentrations of 100 mg/mL BSA, 50 mM NaPS, 100 μ M Ru(BiPy)₃, and 3 mM DTT.

View Article Online
DOI: 10.1039/D4FD00204K

Rheology

Rheology was performed to characterise the mechanical properties of the hydrogels *in situ* by an Anton Paar MCR 302 rheometer using a parallel plate geometry (8 mm diameter). The pre-gel solution was loaded on the rheometer, and the gap height was adjusted for each measurement to ensure correct sample filling. Then, a thin layer of silicon oil was pipetted at the edges of the pre-gel solution to avoid any sample evaporation. Measurements were carried out at 20°C. A blue LED light source operating at a current of 0.48 A, was turned on, initiating gelation (by photochemical crosslinking)(70,80) and was turned off after 5 min, completing gelation. Time sweep (oscillation) experiments were performed at a constant frequency of 1 Hz and a shear strain of 0.5%. The measurements continued for 60 min after the lamp was turned off to record relaxation of the samples post-gelation. Frequency sweep measurements were acquired over the range of 0.1 to 2 Hz. Following the method described by Hughes *et al.*, the relaxation exponent n is extracted by fitting a linear function to the frequency sweeps(70):

$$\log(G') = n \log(f) + \log(A) \quad (1)$$

Where G' and f are the corresponding elastic modulus and oscillation frequency of the measurement, n is the relaxation exponent, and A is a prefactor.

Cryo-SEM sample preparation

Slush nitrogen freezing

Two different sample preparations were used to explore the effect of sample thickness on resulting structures. Samples were either gelled (irradiated with a 20 W LED projector of 452 nm wavelength for 5 min) inside a 10 mm wide and 5 mm deep sample holder (*in-situ* sample preparation) or on a petri dish, fractured with a surgical knife and placed in the sample holder (*ex-situ* sample preparation). For the *ex-situ* hydrogels, the void space in the sample holder was filled by a mixture of optimum cutting temperature (OCT) compound and carbon paste, ensuring good thermal and electrical conductivity across the loaded holder. All hydrogels were frozen by quickly immersing the gels into slush nitrogen held at -207 °C.

High pressure freezing

All samples were directly gelled (irradiated with a 20 W LED projector of 452 nm wavelength for 5 min) into 100 μ m deep planchettes of 3 mm diameter, leaving no void space. The planchette containing the sample is placed in a planchette holder with a hole in it. A second flat lipid-coated planchette was placed directly over the first planchette to secure the gel and form the pressure chamber. The planchette holder containing both planchettes is secured between two identical half cylinders. Then, the samples were high pressure frozen using a Leica EM ICE. After freezing, the high pressure frozen samples (placed in the frozen planchettes secured inside the planchette holder and the half cylinders) were placed under liquid nitrogen inside a sample unloading chamber, which contains a sample release station, filled with liquid nitrogen. The planchette holders with the two frozen planchettes (attached to each other) are transferred to the sample release station. The frozen planchettes are punched out from the holder under liquid nitrogen using a release handle separating them. The 100 μ m deep frozen planchettes containing the high pressure frozen samples are collected and stored under liquid nitrogen. Before transfer to the SEM, the frozen samples were mounted onto a Quorum sample holder with two collets under liquid nitrogen to prevent samples from warming.



Cryo-SEM imaging

The structural features of the hydrogels were plasma focused ion beam (pFIB) milled and imaged at cryogenic temperatures using a TESCAN AMBER X Plasma FIB-SEM. The frozen hydrogels were transferred onto a cooled specimen stage held at $-140\text{ }^{\circ}\text{C}$ inside a Quorum cryo-preparation chamber under high vacuum (10^{-7} mbar). An anti-contaminator was cooled to $-170\text{ }^{\circ}\text{C}$ to reduce frost contamination. The slush frozen hydrogels were fractured using a cold knife and sublimed at $-70\text{ }^{\circ}\text{C}$ for 5 min to expose the internal features of the gels and then vacuum transferred into the imaging chamber of the SEM. In an alternative route to expose the inner structure of the HPF hydrogels, pFIB milling with a 10 nA probe was conducted to mill a $30 \times 30 \times 20$ mm (width x height x depth) volume of sample (microscope details are given below). The front side of the milled trench was further polished using a 1 nA pFIB probe to reveal an unaltered face of pristine gel. Then, the HPF samples were sublimed at $-100\text{ }^{\circ}\text{C}$ for 8 min to expose the pores of the hydrogels. All samples were surface sputter-coated with platinum at 5 mA for 45 s to enhance their conductivity and reduce thermal damage and charging. The samples were transferred inside the SEM chamber under high vacuum at $-140\text{ }^{\circ}\text{C}$. Images were taken at a range of magnifications with a probe current of 100 pA and beam energy of 2 kV (to minimise irradiation damage). Elemental mapping of hydrated sample surface was conducted using an Oxford Instruments Aztec Energy Dispersive X-ray (EDX) Spectroscopy system.

View Article Online

DOI: 10.1039/D4FD00204K

Image Analysis

The ImageJ software,⁽⁸⁴⁾ was used for pore size, wall thickness, cluster size and intercluster distance analysis. Image segmentation was conducted for the pore size measurements. In detail, a contrast threshold is set at around 35-45%, depending on the contrast of the image pre-processing, to put background signal (i.e. pores) to black and preserve only morphological information as white. After that, 'watershed' and 'fill holes' analysis tools are selected to automatically separate and cut 'particles' that touch and fill any remaining holes that could affect the measurements. The Feret's diameter was assigned for the pore length. Pores caused due to beam damage were excluded from the measurements (Figure S1 shows an increase in pore sizes due to prolonged exposure by the electron beam). For visualisation of the protein clusters and intercluster distances, enhanced contrast images were obtained by narrowing the contrast and brightness limits of the image to reveal signal from the front layer of the sample. Standard errors are used, and data are shown by mean \pm standard error of the mean.

Results and Discussion

Rheology of folded protein hydrogels

In order to confirm successful gelation of BSA hydrogels, elastic (storage) (G') and viscous (loss) (G'') moduli were measured against time *in-situ* (Figure 2a). A time sweep monitoring the gelation of a photochemically cross-linked 7.4% (volume fraction) folded BSA hydrogel is displayed in Figure 2b. This time sweep behaviour has previously been reported for *in situ* gelation studies on folded BSA gels.^(70,73,81–83) The gelation curve shows the evolution of G' and G'' with time when a lamp is switched on at $t = 0$ s, initiating gelation, switched off at $t = 300$ s, completing gelation, and during network relaxation up to $t = 3960$ s. Initially, a sharp increase in G' is displayed due to photo-activated crosslinking gelation of the BSA protein into a network, which then decreases due to network relaxation, reaching a time-stable plateau value. The time at which $G' = G''$ ($t = 21$ s) indicates the gelation point as the sample transitions into a viscoelastic gel.

The frequency sweeps displayed in Figure 2c and d show G' , G'' and the loss ratio $\tan(\delta)$ (defined as G''/G') variation versus oscillation frequency. Both elastic and viscous components increase with increased frequency. Fitting a linear function to the G' data of Figure 2c, between 0.1 and 2 Hz, enables a relaxation exponent n to be calculated.⁽⁷⁰⁾ We measured n for the folded BSA hydrogels to be



0.029 ± 0.0002, indicating that the gels have elastically dominated behaviour (n for a viscous hydrogel approaches 1, whereas that of an elastic hydrogel approaches 0). This is also supported by the loss ratio $\tan(\delta)$, which has a value below 0.1 ($\tan(\delta)$ is defined as G''/G' , so when $\tan(\delta)$ is below 1, the gel exhibits elastically dominated solid-like behaviour, whereas, when $\tan\delta$ is higher than 1, the gel displays a liquid-like behaviour).

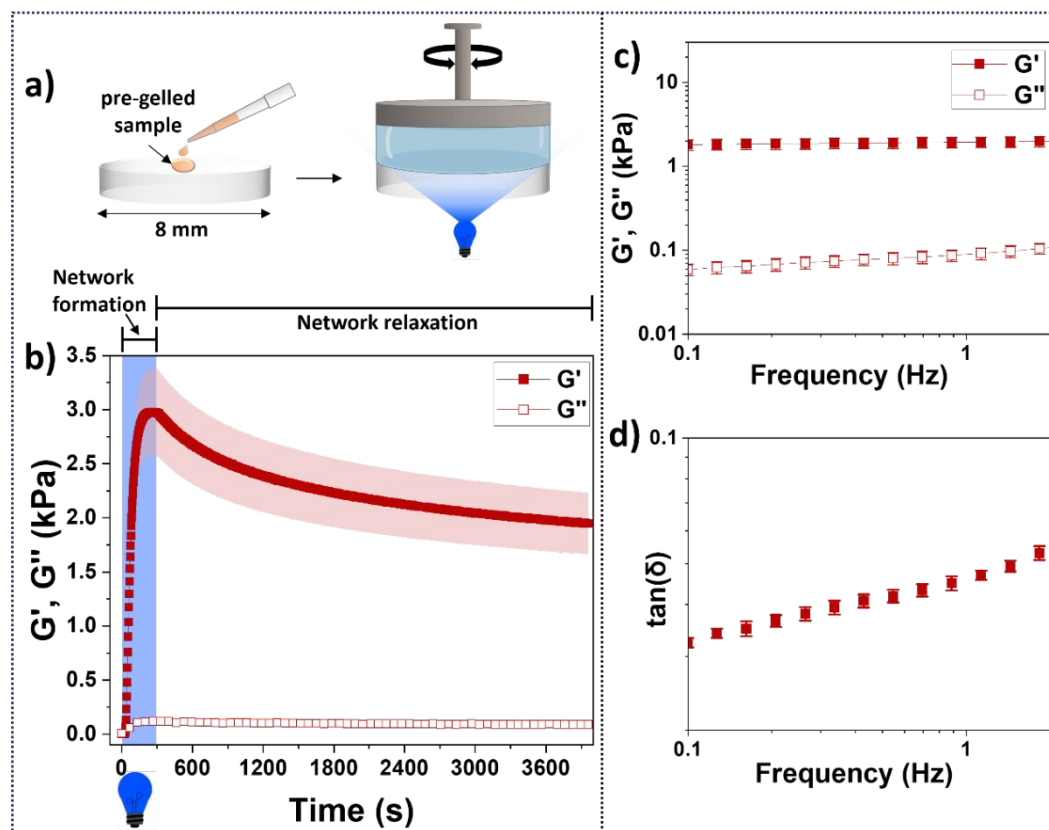


Figure 2. a) Schematic of sample preparation, parallel plate geometry and measurements for the folded BSA (7.4% BSA) hydrogel rheology. The pre-gelled sample is placed on top of a glass surface, and blue light illumination from below is used for photoactivated gelation. b) Time sweep rheology measurements confirm successful gelation. Gelation curves showing the changes in the elastic G' and viscous G'' moduli against time at 1 Hz. At $t = 0$ s, the lamp is turned on, initiating gelation. After 300 s, the lamp is turned off, completing gelation (highlighted by blue light). The measurements were done in real time, monitoring the formation and relaxation behaviour of the hydrogel. b) Frequency sweep measurements of G' , G'' and c) the loss ratio, $\tan(\delta)$ of the photochemically crosslinked gels. Filled symbols represent the storage modulus (G'), and the open symbols the loss modulus (G''). The error ribbons (b) and bars (c,d) display the standard errors calculated after 3 repeats.

Small angle scattering (SAS) reveals mesoscale structure for complementing cryo-SEM

Small angle neutron scattering (SANS) and small angle X-ray scattering (SAXS) are used to probe network structure on length scales between tens to hundreds of Angstroms to study the structure of hydrogels,⁽¹⁴⁾ including photochemically cross-linked protein hydrogels. SAS provides the opportunity to extract *in-situ* bulk measurements of a system (Figure 3a). The data shown in Figure 3b and c show SAXS and SANS for folded BSA hydrogels (7.4% BSA) prepared in the same way as the present study.⁽⁷⁰⁾ The SANS experiments were completed in a 35% D_2O /65% H_2O solution, while the SAXS experiments for folded BSA hydrogels (Figure 3 a and c) were completed in the Nano-inXider



instrument at the ISIS neutron and Muon Source (concentration: 7.4% BSA, 20 mM NaPS, 100 μ M Ru(BiPy)₃ in a 100% H₂O).(70) Differences are observed in the background scattering in the SANS data compared to the SAXS data, as expected, due to the higher incoherent scattering from the hydrogen in the buffer in SANS which is not a consideration in SAXS. SANS and SAXS experiments have previously shown that these folded BSA hydrogels form heterogeneous network structures with fractal-like clusters connected by more sparsely populated intercluster regions of folded proteins (**Figure 3d**).(70,81–83) .

A fractal structure factor model(85) can be used to extract quantitative information from the scattering curves(70) (see SI). From this model, two key structural parameters are obtained: the fractal dimension, D_f , which is a measure of the space-filling capacity of an object and here can be thought of as the density of a cluster; and the characteristic or correlation length of the fractal-like clusters, ξ , which is related to the overall size of the clusters. Details regarding the SAS models and formulas are explained in the SI.

Previous SAS studies on BSA-based hydrogels have applied the fractal structure factor model and found that in the presence of DTT, the clusters become denser and larger (approximately 7 times more protein in each cluster), and the intercluster region sparser, suggesting a more heterogeneous network.(70,83) It was shown that regardless of the presence of DTT, a heterogeneous hydrogel network dominated by clusters of proteins is formed. Inspired by this, cryo-SEM was used to explore BSA-based hydrogels to understand what features of the SAS structural models can be resolved by electron microscopy.



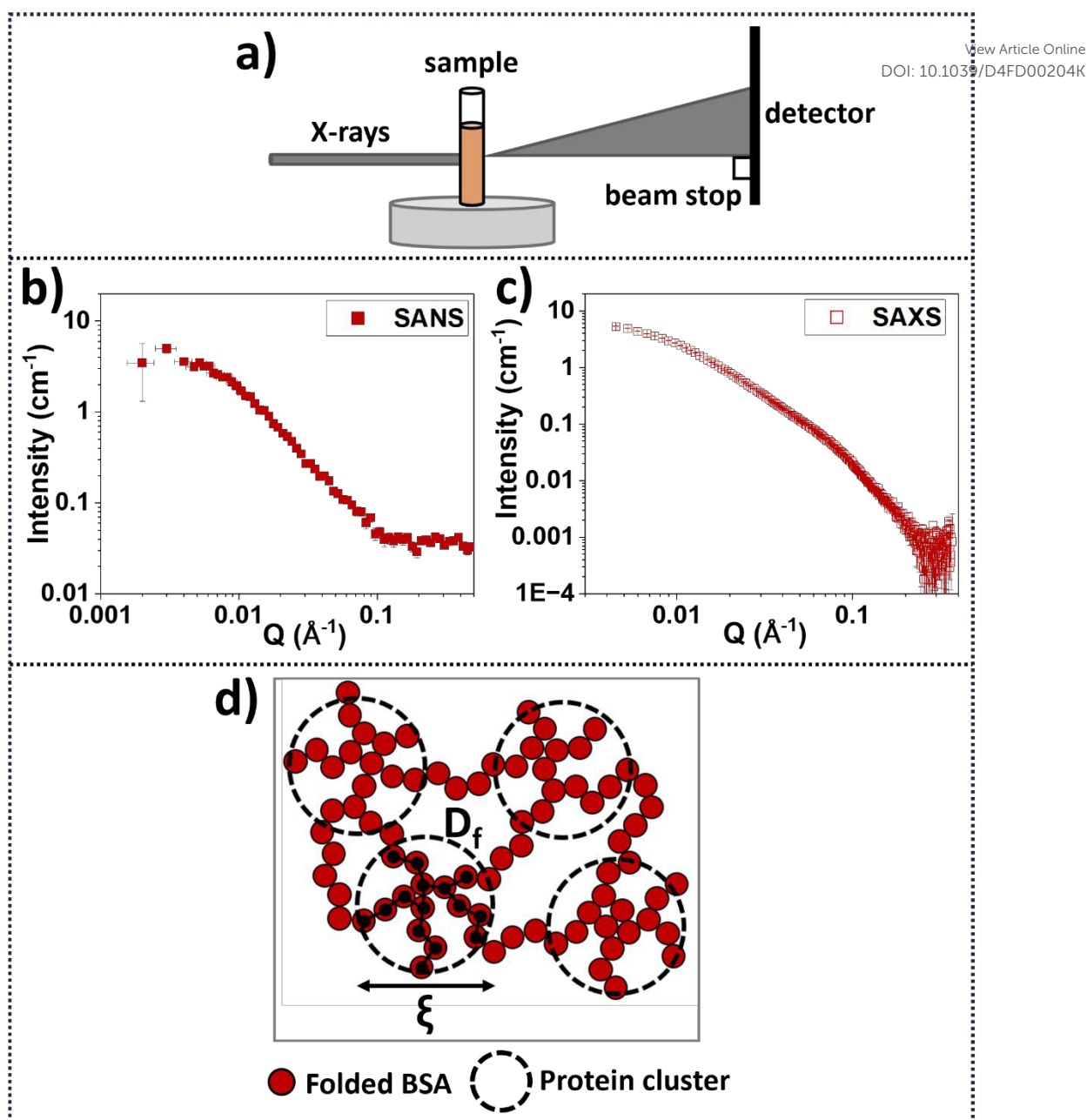


Figure 3. a) Schematic of SAXS data acquisition geometry. The accessible q -range investigated was $0.0045\text{--}0.37 \text{ \AA}^{-1}$ and $0.002\text{--}0.5 \text{ \AA}^{-1}$ for SAXS and SANS, respectively. Samples were directly gelled inside sample holders. b) SANS data from the Sans2d instrument at the ISIS neutron and Muon Source, UK, for folded BSA hydrogels (concentration: 7.4% BSA, 20 mM NaPS, $100 \mu\text{M Ru}(\text{BiPy})_3$ in a 35% $\text{D}_2\text{O}/65\%$ H_2O and c) SAXS data from Nano-inXider instrument at the ISIS neutron and Muon Source for folded BSA hydrogels (concentration: 7.4% BSA, 20 mM NaPS, $100 \mu\text{M Ru}(\text{BiPy})_3$ in a 35% $\text{D}_2\text{O}/65\%$ H_2O). (70) d) Schematic of the predicted network structure using SANS and SAXS using model fitting of data from reference(70) suggesting that the network consists of connected clusters made by folded protein. Correlation length ξ is indicative of the cluster size, and the fractal dimension D_f can be thought of as the density of the cluster.



Cryo-SEM imaging using the slush nitrogen cryofixation method

View Article Online

DOI: 10.1039/D4FD00204K

Exploring the effect of different sample handling on the pore sizes of folded protein-based hydrogels

In order to establish an EM methodology to obtain images of folded protein-based hydrogels, slush nitrogen freezing was first explored, as this method has been used many times before to image BSA-based systems with reports of a characteristic honeycomb-like structure.(37–39,86,87) However, previous studies have highlighted that the low vitrification depth of slush/liquid nitrogen freezing introduces artefacts in polymer-based and heat-induced protein-based hydrogels.(28,50) Motivated by this, we evaluated potential artefacts of this cryofixation method on folded protein hydrogels.

Two different sample preparation routes of the same gel but of different thicknesses prior to freezing in slush nitrogen were investigated, as sample thickness can affect ice crystal growth.(88) For the *in-situ* sample preparation (**Figure 4a**) a sample is gelled in the sample holder and frozen ‘in bulk’. In contrast, for the *ex-situ* route (**Figure 4b**) an already gelled sample is sectioned to be less thick than the *in-situ* gel preparation sample, and then placed in a holder for freezing.

Cryo-SEM images of the *in-situ* and *ex-situ* samples after sublimation are displayed in **Figure 4c** and **Figure 4d**, respectively. Both preparation routes display a honeycomb-like structure commonly reported for BSA-based systems.(37–39,86,87) The average pore length for the *in-situ* sample is $5.26 \pm 0.05 \mu\text{m}$ and is \sim six times shorter for the *ex-situ* sample, $0.72 \pm 0.01 \mu\text{m}$. Clearly, the scale of the pore sizes depends on the preparation route, and it is suggested that this is due to specimen thickness affecting ice crystal formation. i.e., the honeycomb-like structure observed is not the native network of the gels but is caused by ice crystal formation and protein displacement to the boundaries of the crystals as they nucleate and grow.

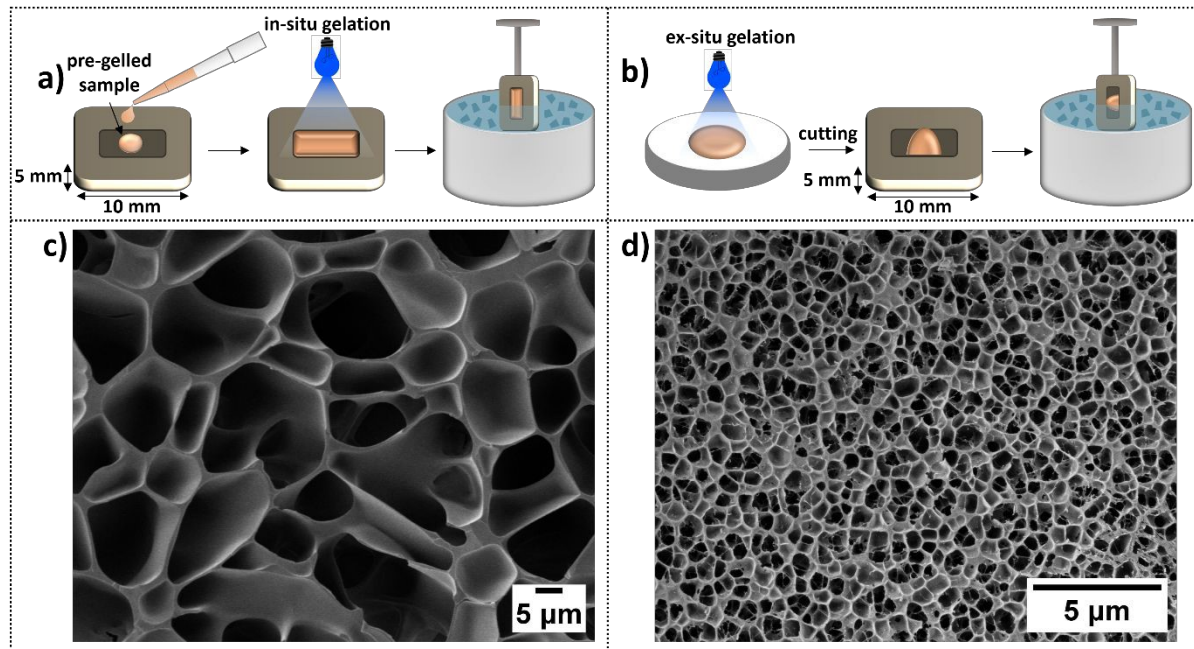


Figure 4. a) Schematic of the *in-situ* sample preparation route, which consists of directly gelling the sample in the cryo-holder before freezing in slush nitrogen. This route produces a sample thicker than $5 \mu\text{m}$ but does not require sectioning of a non-frozen gel i.e. eliminates any potential structural alteration due to knife-induced tearing or shearing. b) Schematic of the *ex-situ* sample preparation route, which consists of gelling the sample in a petri dish, cutting off a thin section, which is then transferred into a cryo-holder before freezing in slush nitrogen. This route creates a thinner sample than *in-situ* preparation but still thicker than $5 \mu\text{m}$. (c-d) Cryo-SEM images of sublimed BSA hydrogels



(7.4% BSA protein hydrogel) frozen in slush nitrogen, prepared a) *in-situ* and b) *ex-situ*, highlighting pore formation suspected to be due to insufficient vitrification.

View Article Online
DOI: 10.1039/D4FD00204K

Exploring the effect of the imaging area on the structure of folded protein-based hydrogels

To further investigate and support that slush nitrogen freezing inhibits complete vitrification of water inside hydrogels, cryo-SEM images were acquired at the edge and towards the centre of the holder (more than 100 μm from sample edge) of the slush frozen and sublimed BSA hydrogel prepared *in-situ* (7.4% BSA protein hydrogel) (**Figure 5a** and **b**). There is a clear porosity change from the edge to the bulk of the sample (**Figure 5c**), particularly across the expected 2-5 μm limit for complete vitrification of a slush frozen hydrogel.⁽⁵⁰⁾ The average pore length at the edge of the sample was 129 ± 3 nm whereas beyond a depth of ~ 5 μm , the slow cooling rate provides enough time for ice crystals to nucleate and grow, altering the network into a honeycomb structure with ~ 1 -10 μm size pores after sublimation. Thus, we can conclude that the pores observed in **Figure 4c** and **d** and **Figure 5a** and **c** are induced by ice crystal formation, and the walls are made of protein that has been pushed to the boundaries of the growing ice crystals⁽⁸⁹⁾.

It is also noted here that slush nitrogen freezing provides sufficient time for ice crystals to form within hydrogels regardless of the building block used. For example, Efthymiou *et al.* highlighted this issue when imaging heat-induced protein and polysaccharide-based hydrogels.⁽²⁸⁾ Buchheim also supports this, reporting that hydrogels containing more than 80% water are expected to show structural damage due to ice crystal formation, with crystal sizes at the μm scale.⁽⁹⁰⁾ The slush/liquid nitrogen freezing method has been used to induce ice crystal formation and create pores in hydrogels for use as scaffolds in tissue engineering applications.⁽⁹¹⁾ It is even clear that by modifying the cooling rate, the internal porous architecture of hydrogels can be adjusted^(92–94) so that if the water is sublimed, a microporous network is formed, whose size and morphology are determined by the freezing rate, temperature and sublimation conditions.^(95–97)

Occasionally, we observed a second porous network interconnected within the larger honeycomb-like voids, as shown in **Figure 5d**, which has also been reported by Aston *et al.* in alginate-based gels.⁽⁵⁰⁾ This smaller network appeared as thin fibres within the larger pores. The average length of the smaller pores was 192 ± 6 nm.



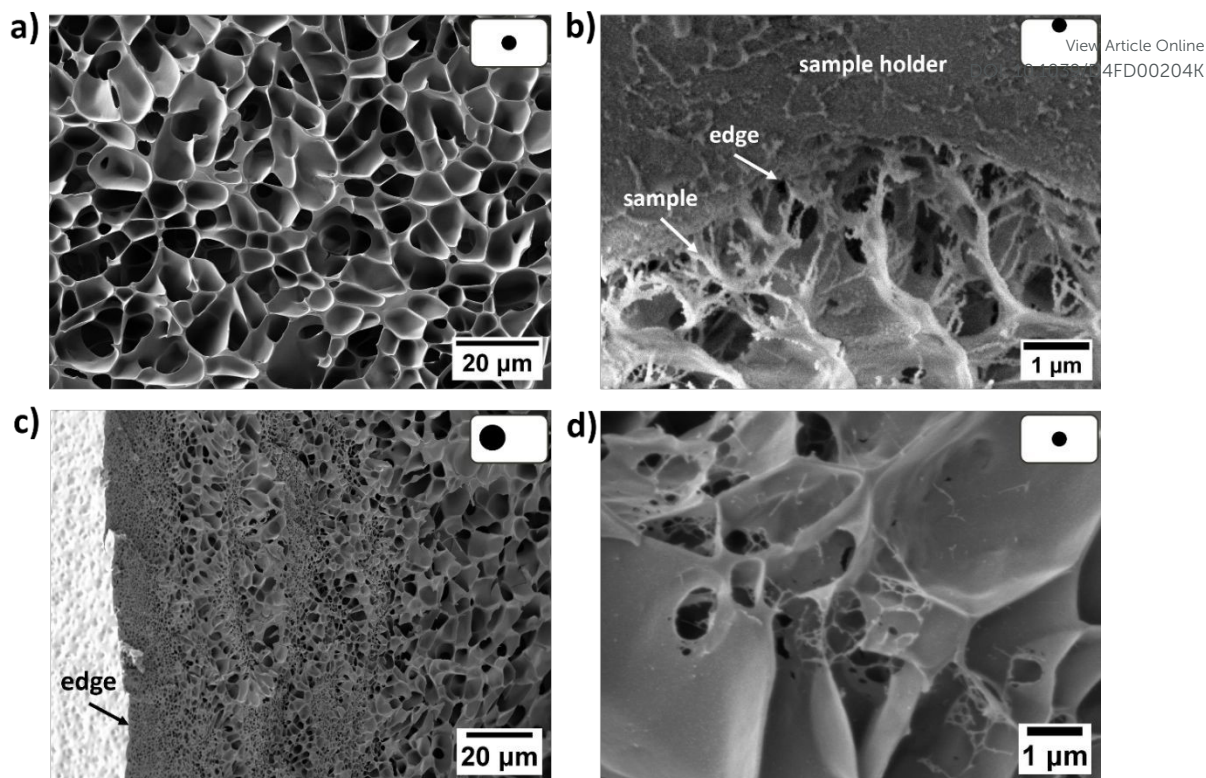


Figure 5. Cryo-SEM images of a slush frozen, sublimed folded BSA hydrogel (7.4% BSA) prepared *in-situ* prior to freezing taken from a) the middle and b) at the edge of the sample. c) Decreased magnification (zoom out) image of the hydrogel highlighting the pore size difference between the edge and bulk of the hydrogel. d) A secondary, smaller porous structure is sometimes seen within the larger pores. The location of the imaging sites within the cryo-holder is shown on the top right of each image (black dot within a white rectangle).

EDX elemental mapping of hydrated folded protein-based hydrogels

To further investigate ice crystal formation, energy dispersive X-ray spectroscopy (EDX) based elemental mapping was conducted on a slush frozen but hydrated, folded BSA hydrogel (7.4% BSA) prepared *ex-situ*. An elemental map of the hydrated gel is displayed in **Figure 6a**. Oxygen (O) is detected throughout the sample while carbon (C) is detected at the walls of the network suggesting water does indeed fill the voids while the proteins are located at the walls. Sodium (Na) was detected in the network walls and is found in the reagent stock used for the gelation, confirming that ice-crystal nucleation and growth do push all impurities to the walls of the network.

A high magnification cryo-SEM image of a slush frozen, hydrated folded BSA hydrogel (7.4% BSA) prepared *ex-situ* prior to freezing is displayed in **Figure 6b**. Clusters 29.8 ± 0.4 nm connected together in a sub-network structure within the walls of the frozen gel are clearly visible. Even though these clusters are compressed together at the pore walls, the undeformed network structure is similar to that predicted by modelling of SAS data (**Figure 3c**) (70). Figure 6 indicates what can be achieved by elemental mapping and high-resolution imaging with the appropriate cryo-SEM sample preparation.



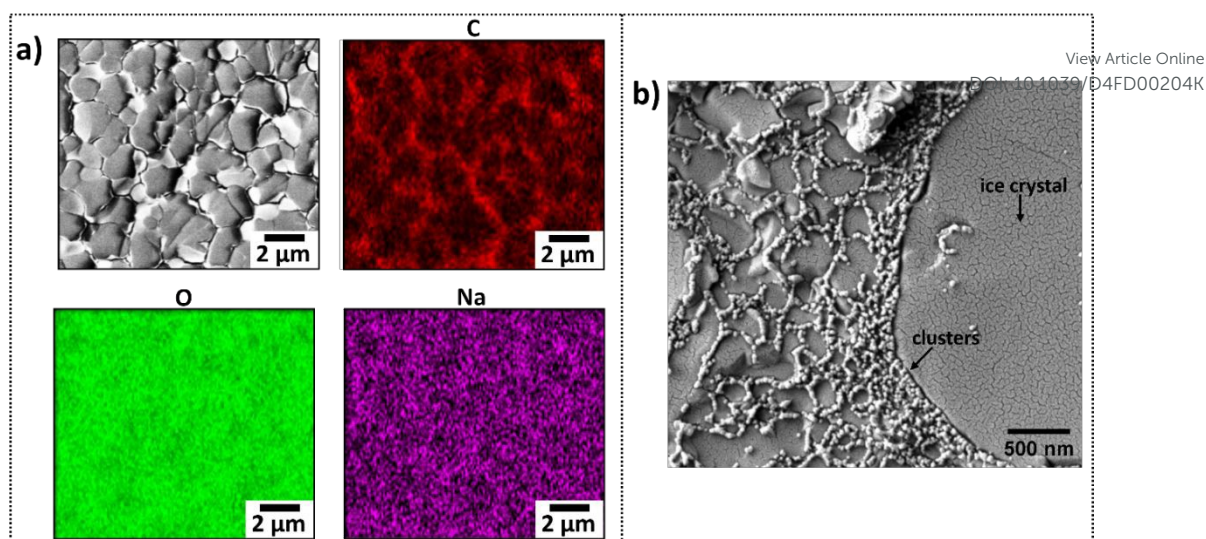


Figure 6. a) Elemental mapping by EDX spectroscopy of a slush frozen, hydrated, folded BSA hydrogel (7.4% BSA) prepared *ex-situ* prior to freezing. Assigned elements are labelled on top of each image. b) High magnification cryo-SEM image of the same hydrogel displaying a network wall structure of interconnected clusters that have been displaced to the boundaries of the ice filled pores.

Cryo-SEM imaging using the high-pressure freezing (HPF) cryofixation method

Investigation of folded protein-based hydrogels

HPF enables vitreous freezing of hydrogels up to 500 μm thick.⁽⁴⁵⁾ Here, HPF was used to freeze 100 μm thick samples first prepared by gelling *in-situ* (Figure 7a) in order to explore the structure of folded protein-based hydrogels without ice crystal formation. Figure 7b-d show the required steps to expose the porous structure of the hydrogels. In more detail, cryo-plasma focused ion beam (pFIB) milling (Figure 7b) was conducted on the HPF samples to expose the native structure of the hydrogels. pFIB milling was preferred over knife sectioning in order to eliminate the risk of mechanical damage such as knife induced compression, tearing, lift-out and drag^(98,99), which we have observed in sectioned hydrogel samples (Figure S2). We minimised ion/plasma beam artefacts, such as excessive curtaining due to over-milling, by careful control of the final cleaning currents and times (example of over-milling shown in Figure S3). Sublimation was still required to expose the porous network structure of a carefully ion milled face (Figure 7c and d).

A high magnification cryo-SEM image of a HPF, pFIB milled and sublimed, folded BSA (7.4% BSA) hydrogel is shown in Figure 7d. The structure difference between the hydrogels frozen by HPF and in slush nitrogen is striking (Figure 4 vs Figure 7). The pores of the HPF samples appear rounded, are 58.3 ± 0.2 nm across and are two orders of magnitude smaller than the pores in the bulk regions of the slush nitrogen frozen hydrogels (5.26 ± 0.05 μm).

The pore sizes and heterogenous network structure measured by the HPF sample preparation are similar but smaller to those within 2-5 μm of the edge of the slush frozen gel (and similar to the secondary networks seen within some pores of the bulk slush frozen gel; Figures 5c and d). Aston et al. observed a similar behaviour in alginate-based hydrogels.⁽⁵⁰⁾



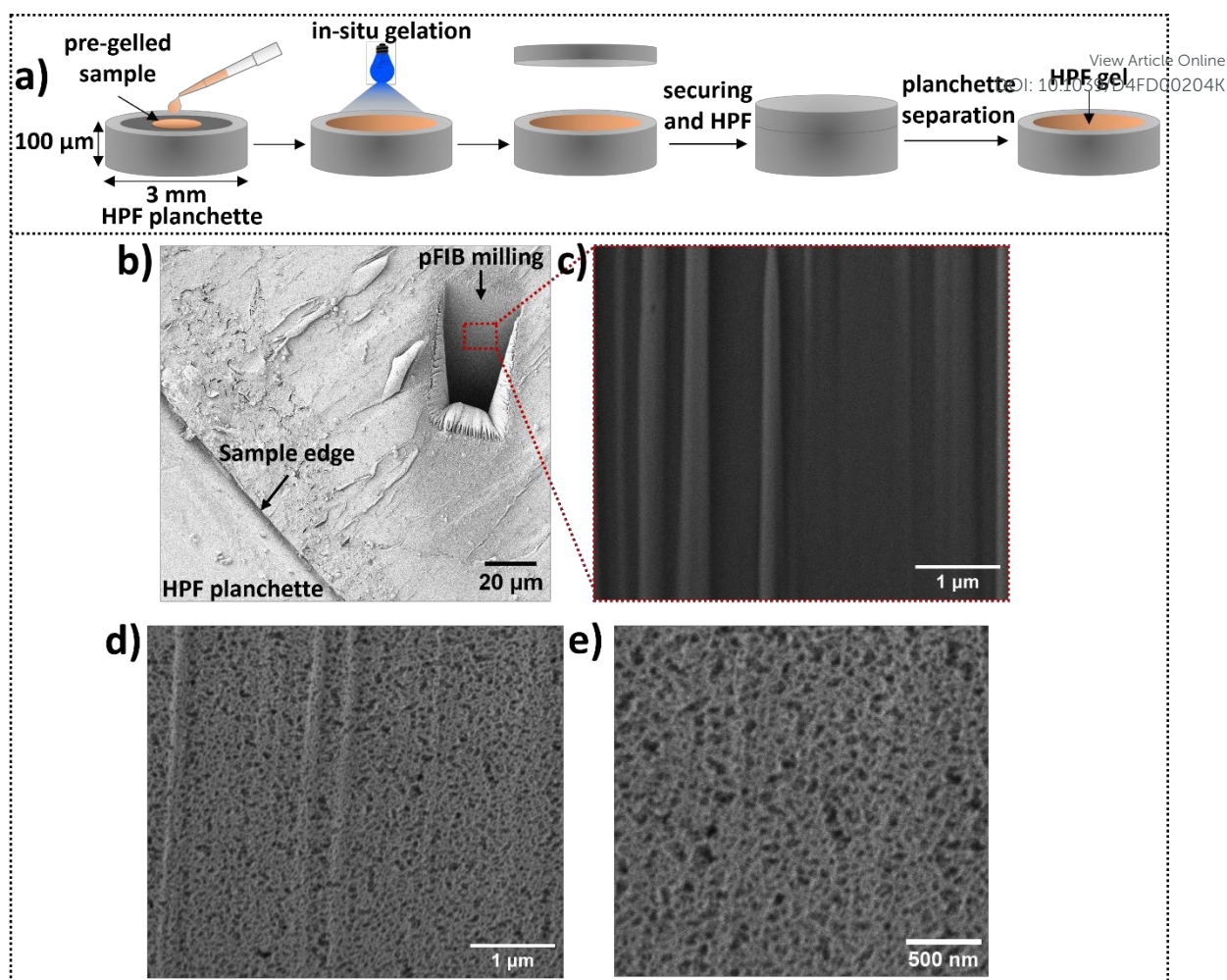


Figure 7. The methodology used to acquire an image of an HPF, pFIB milled and sublimed folded BSA hydrogel (7.4% BSA) prepared *in-situ* prior to HPF. a) Schematic representation of the *in-situ* sample preparation. The sample is directly gelled into a 100 µm deep planchette, leaving no void space. Then, a second flat planchette is placed on top, securing the sample prior to HPF. After HPF, the planchettes are separated, exposing the frozen, hydrated gel. (b-e) Cryo-SEM images of the HPF BSA hydrogel after: b) pFIB milling was used to expose the inner structure of the hydrogels; (c-d) Images obtained from the front side of the milled area c) before and d) after sublimation exposing the pores; e) Increased magnification of the milled area after sublimation.

Image analysis exploration of folded protein-based hydrogels

Cryofixation without devitrification of ice (by HPF) offers a powerful opportunity for image analysis exploration. Our methodology to obtain cryo-SEM images of folded protein-based hydrogels containing high amounts of water is captured in **Figure 8a**. The route consists of *in-situ* gelation to ensure native gel state preservation, HPF for cryofixation with water vitrification and little or no ice crystal formation, pFIB milling to avoid knife compression and then sublimation to expose the native structure of the hydrogels.

Low current, low kV secondary electron imaging of the cryo-fixed hydrogels is required to reveal pores within a network composed of regions of high secondary electron emission connected by narrower, lower emission regions. **Figure 8bi** is a high contrast version of the image in **Figure 7e** and in this we can assign the regions of high secondary electron emission as clusters (highlighted as orange spheres) and the lengths across the lower emission regions as intercluster distances (highlighted as green lines). The average cluster diameter is 30.1 ± 0.6 nm and the intercluster distance 20 ± 1 nm. From SANS



data, the extracted correlation length ξ for BSA hydrogels was 12.3 nm, which is indicative of the average cluster size across the whole network.⁽⁷⁰⁾ Interestingly, the value of ξ is the same order of magnitude as the individual protein cluster diameter directly measured in the cryo-SEM images of the hydrogel network. While models are required to obtain the network structure from SANS data, cryo-SEM is a powerful method to directly visualise the heterogeneous network and complement SAS derived models to gain valuable information regarding the pore structure of folded-based hydrogels.

Network pore sizes can be obtained by thresholding the image of **Figure 7e** such that pores have black contrast and any other structure has white contrast (using Image J software and shown in **Figure 8b ii**). The average pore size of the folded BSA gel is 58.3 ± 0.2 nm. We confirm that low electron doses are required to keep the network integrity and not alter the pore size distributions by demonstrating an increase in measured pore size and pore size distribution with prolonged irradiation of the sample (**Figure S1**).

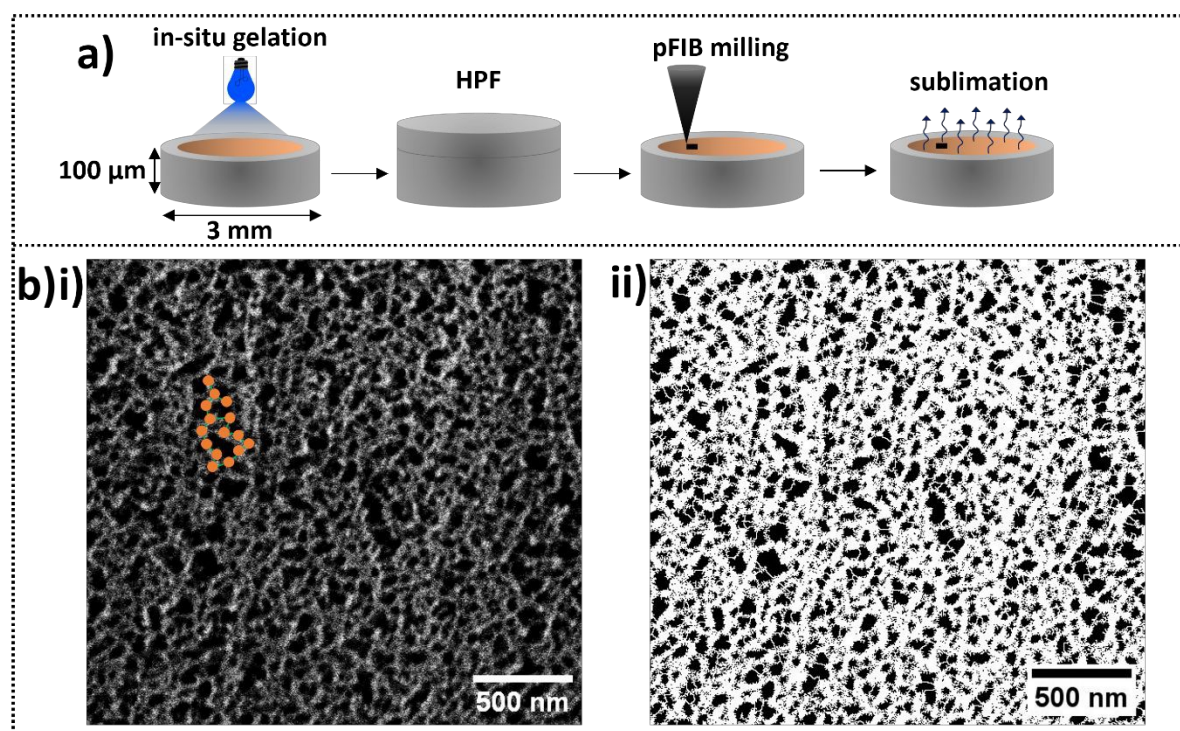


Figure 8. a) Schematic of a route for obtaining representative images of cryo-fixed hydrogels. The steps consist of in-situ gelation ensuring no mechanical structural alteration, HPF assuring vitreous freezing, pFIB milling to expose the inner structure and sublimation to expose the pores and structural features of the hydrogels. b) Processed high magnification images of a folded BSA hydrogel (7.4% BSA) prepared following the steps in panel a, highlighting image analysis possibilities. bi) High contrast image for cluster (orange) and intercluster distance (green) measurements. bii) Threshold image for pore size (black voids) analysis.

Investigation of nanoscale protein manipulation on the structure of protein-based hydrogels

After establishing a methodology for obtaining representative EM images of the native structure of folded protein-based hydrogels containing high amounts of water, the effect of protein unfolding on the network architecture of the hydrogels was explored. This is motivated by the growing interest in the use of force-sensitive proteins in the design and mechanosensing of biomaterials.^(1,71)

BSA is an ideal model protein due to its mechanical ‘nanostaples’ preventing BSA from unfolding. The addition of DTT allows BSA to unfold during gelation, and this has an impact on the structure and



mechanics of the hydrogel network, as shown schematically in **Figure 9a**.(70) From previous SANS studies of a 7.4% BSA hydrogel(70), it was found that the measured fractal dimension D_f of a cross-linked cluster is larger in BSA hydrogels formed in the presence of DTT ($D_f = 2.66$ in the presence and 2.17 in the absence of DTT). The correlation length, which is indicative of the cluster size, also increases in the presence of DTT ($\xi = 123$ Å in the absence of DTT and 130 Å in the presence of DTT). More recently, SAXS studies of a 7.4% BSA hydrogel used a model-independent Guinier-Porod fits to SAXS curves to extract the Porod exponent and the radius of gyration of the largest scattering object.(82) (*Hughes et al.*, *Soft Matter*, under review) The data showed $R_g = 140$ Å and $D_f = 2.5$ in the absence of DTT(82) and $R_g = 200$ Å and $D_f = 2.8$ in the presence of DTT. (*Hughes et al.*, *Soft Matter*, under review) Application of the fractal structure factor model to the SAXS data yielded a $\xi = 116$ Å and $D_f = 2.48$ in the absence of DTT and $\xi = 166$ Å and $D_f = 2.75$ in the presence of DTT. (*Hughes et al.*, *Soft Matter*, under review) Whilst the exact numbers show differences, in all cases, BSA hydrogels in the presence of DTT show an increase in R_g , ξ and D_f . Taken together, this suggests that hydrogels made from force-labile BSA (nanostaples removed) form denser fractal-like clusters of larger size compared to the clusters present in hydrogels made from mechanically robust BSA (nanostaples present). Cryo-SEM has the potential to directly visualise these structural changes upon protein unfolding while also observing the induced changes to pore sizes within the protein hydrogel architectures.

High magnification and contrast adjusted images of the structure of mechanically robust BSA (nanostaples present) and force-labile BSA (nanostaples removed) hydrogels prepared by our methodology (Figure 8a) are displayed in **Figure 9b** and **c**, respectively. For both systems, a heterogeneous network is observed with porosity directly visible within a network dominated by clusters and intercluster connections or 'walls'. The average cluster diameters, highlighted as orange spheres in **Figure 9b** and **c** were measured to be 30.1 ± 0.6 nm and 44.2 ± 0.6 nm in the absence and presence of DTT, respectively. The cluster diameters extracted from cryo-SEM (**Figure 9e**) follow the same trend as those extracted from the SANS data with an increase in cluster diameter for networks made from force labile BSA protein. Intercluster distances, highlighted as green lines in the cryo-SEM images of **Figure 9b** and **c**, are 20 ± 1 nm and 27 ± 2 nm for the mechanically robust and force labile BSA system, respectively (**Figure 9f**).

Whilst it is known that making BSA force labile by protein unfolding during gelation creates a gel network with bigger, more well-spaced protein clusters, we can for the first time, use cryo-SEM to image directly the porosity changes within this structure. The average pore length (**Figure 9d**) is measured to be 58.3 ± 0.2 nm in the absence of DTT, and 67.0 ± 1.4 nm in the presence of DTT, i.e. we can confirm an increase in pore sizes with protein unfolding and visualise the expected increase in heterogeneity of the DTT exposed gels.



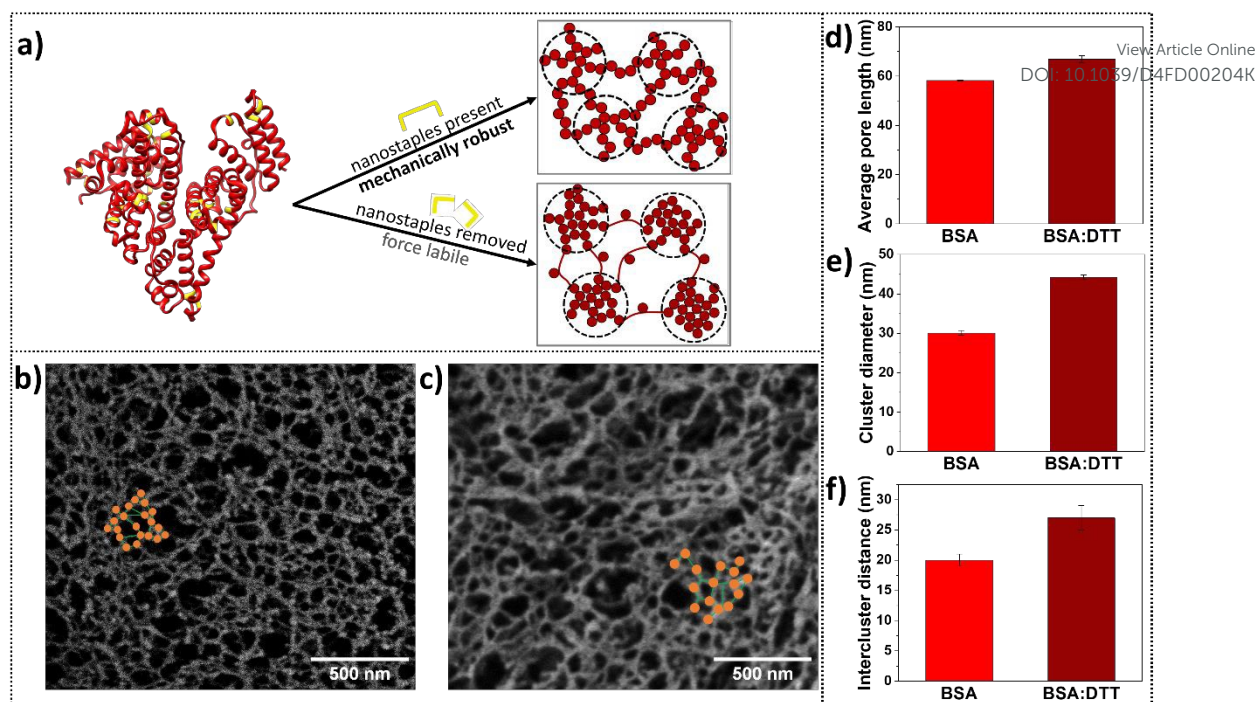


Figure 9. Controlling protein unfolding in-situ influences gel mechanics and structure. *a)* From left to right: Schematic of the 3D structure of BSA highlighting the disulphide bonds (nanostaples) in yellow, which hold BSA in a folded state. The nanostaples preserve the mechanical robustness of the protein. Removal of the nanostaples makes the protein force labile, leading to unfolding during gelation and ultimately to network alteration and a loss of mechanical rigidity. SAS schematics of the corresponding structures highlight structural changes in the network from reference(70). *(b-c)* High contrast cryo-SEM images of HPF, pFIB milled and sublimed prepared in-situ prior to freezing *b)* folded BSA (7.4% BSA) (mechanical robust protein) and *c)* unfolded BSA:DTT (7.4% BSA) (force labile protein) gels, with highlighted image analysis. Orange spheres represent the clusters, and green lines the intercluster distances. *d)* Average pore length of gels made by mechanically robust BSA (light red) and force labile BSA (dark red), as extracted by cryo-SEM images. *e)* Cluster diameter measurements of gels made by mechanically robust BSA (light red) and force labile BSA (dark red) as extracted by cryo-SEM. *f)* Intercluster distance measurements of gels made by mechanically robust BSA (light red) and force labile BSA (dark red) as extracted by cryo-SEM. Error bars display the standard error of the mean.

Overall, we show that appropriate sample preparation for cryo-SEM by HPF of folded protein hydrogels can be used to gain information about the morphology and pore sizes of protein-based systems and image the impact of unfolding in the network through image analysis. We evaluated our cryo-SEM findings by comparing the results with previous SAS studies.(2,70,73,81–83) The importance of such an integrated approach to assess the structure and characteristics (parameters) of a network and even to validate image analysis tools has been highlighted by a number of recent studies.(12,100,101) Often, different parameters can be extracted from different techniques, rendering direct comparison of results challenging. From SAS data, we can extract a radius of gyration R_g , correlation length, ξ , and fractal dimension D_f which are indicative of the lengthscale of the fractal clusters within a network. To directly compare with the cryo-SEM analysis, it will be necessary to measure an ensemble of individual cluster diameters from a number of images. Likewise, it would be powerful if the measure of pore sizes obtained by cryo-SEM could be compared to the porosity in the protein hydrogels studied using SAS. This highlights the importance of retrieving equivalent parameters and understanding how extracted parameters of different techniques can correlate to each other. As this comparison develops, the combination of SAS and cryo-SEM data for the study of protein hydrogels provides an opportunity to understand both the hierarchical structure of the protein



network and the resulting pore sizes of the hydrogel, both of which are critical parameters that describe the heterogeneity of the gel as a whole and give rise to much of its function.

[View Article Online](#)
DOI: 10.1039/D4FD00204K

An additional critical factor for extracting key parameters of the system, such as cluster diameter and intercluster distances, is to develop automated approaches that could measure these parameters from the images obtained, reducing potential bias and time-consuming methods such as manual measurements. The importance of developing image analysis tools that could be applied to these systems has been underlined in fibrous networks by a comprehensive overview and comparison of available automated tools for quantifying characteristics of fibrous networks, such as fibre diameter and length.⁽¹⁰²⁾ Current state-of-the-art image analysis approaches of other microscopy techniques could provide insights for developing similar cryo-SEM analysis tools. In confocal microscopy, studies have developed methods to extract the pore size distribution of polymeric networks in 2-D images by placing circles (or bubbles) of the maximum diameter that could fit the pores until full coverage is achieved.^(103–105) At the same time, in super-resolution microscopy, studies have started to implement new computational methods for data quantification and interpretation due to rapid imaging advances in the field.⁽¹⁰¹⁾ For stimulated emission depletion (STED) microscopy, image autocorrelation analysis was employed to quantify the spatial distribution of fluorophores.⁽¹⁰⁶⁾ Super-resolution diffusion maps have been used to estimate pore sizes of polymeric-based hydrogels.⁽¹⁰⁷⁾

Ultimately, imaging network pores by cryo-SEM opens the possibility of directly accessing information on network architectures and the role of perturbations such as protein unfolding on those structures. For example, a recent study has demonstrated the potential of active particles in ‘kneading’ three-dimensional hydrogels into porous structures.⁽¹⁰⁸⁾ Such studies offer the potential to create a diversity of heterogeneous, percolated porous networks which would be exploited for new functional and response biomaterials. The application of cryo-SEM of appropriately prepared samples could provide powerful insights into active particle-induced porosity changes in such materials.⁽¹⁰⁸⁾ It is expected that hydrogels will have controlled morphologies across individual building blocks to bulk lengthscales, enabling the creation of complex systems, though with significant advancements still required.⁽¹⁰⁹⁾

Conclusions

In this study, we have developed a reproducible protocol to prepare and image protein-based hydrogels, minimising and overcoming artefacts caused by cryo-SEM. This protocol consists of *in-situ* sample preparation prior to freezing to avoid alterations due to mechanical stressing, high pressure freezing to ensure sufficient vitrification, plasma focussed ion beam milling to avoid network compression and sublimation to expose the native structure of the hydrogels. The protocol measures structural differences in the hydrogel networks formed by folded and unfolded protein-based hydrogels. In order to accurately measure differences in the protein network structure, the first steps for image analysis were conducted such that cryo-SEM reveals a heterogeneous network of a folded protein hydrogel to have nanoscale porosity (~60 nm pores) composed of regions of high protein density (~30 nm diameter) connected by thinner, lower density regions (~20 nm in length). Cryo-SEM also shows that protein unfolding induces an increase in network heterogeneity, including an increase of ~10 nm in average pore sizes. Our findings on sample preparation challenges and solutions for imaging protein-based hydrogels using cryo-SEM ultimately present the opportunity to understand the structure-to-function relationship of many hydrogel systems.

Conflicts of interest

There are no conflicts to declare.



Acknowledgements

The project is supported by the Engineering and Physical Sciences Research Council (EPSRC) Centre for Doctoral Training (CDT) in Molecules to Product grant Ref. EP/S022479/1. The project was supported by a grant from the European Research Council (ERC) (UKRI EP/X023524/1) to L. Dougan. We kindly acknowledge the Leeds Electron Microscopy and Spectroscopy (LEMAS) Centre and the Astbury Centre for Structural Molecular Biology of the University of Leeds for facility access and support. Lastly, all members of the Dougan group are gratefully thanked for their feedback and discussions.

View Article Online

DOI: 10.1039/D4FD00204K

Supplementary Information

Supplementary information is provided in an additional document.

References

1. Mout R, Bretherton RC, Decarreau J, Lee S, Gregorio N, Edman NI, et al. De novo design of modular protein hydrogels with programmable intra- and extracellular viscoelasticity. *Proceedings of the National Academy of Sciences* [Internet]. 2024;121(6):e2309457121. Available from: <https://www.pnas.org/doi/abs/10.1073/pnas.2309457121>
2. Aufderhorst-Roberts A, Hughes MDG, Hare A, Head DA, Kapur N, Brockwell DJ, et al. Reaction Rate Governs the Viscoelasticity and Nanostructure of Folded Protein Hydrogels. *Biomacromolecules* [Internet]. 2020 Oct 12;21(10):4253–60. Available from: <https://doi.org/10.1021/acs.biomac.0c01044>
3. Le Roy H, Song J, Lundberg D, Zhukhovitskiy A V, Johnson JA, McKinley GH, et al. Valence can control the nonexponential viscoelastic relaxation of multivalent reversible gels. *Sci Adv* [Internet]. 2024 Dec 3;10(20):ead15056. Available from: <https://doi.org/10.1126/sciadv.adl5056>
4. Tavakol DN, Tratwal J, Bonini F, Genta M, Campos V, Burch P, et al. Injectable, scalable 3D tissue-engineered model of marrow hematopoiesis. *Biomaterials* [Internet]. 2020;232:119665. Available from: <https://www.sciencedirect.com/science/article/pii/S0142961219307641>
5. Huang Y, Fitzpatrick V, Zheng N, Cheng R, Huang H, Ghezzi C, et al. Self-Folding 3D Silk Biomaterial Rolls to Facilitate Axon and Bone Regeneration. *Adv Healthc Mater* [Internet]. 2020 Sep 1;9(18):2000530. Available from: <https://doi.org/10.1002/adhm.202000530>
6. Yang P, Song H, Qin Y, Huang P, Zhang C, Kong D, et al. Engineering Dendritic-Cell-Based Vaccines and PD-1 Blockade in Self-Assembled Peptide Nanofibrous Hydrogel to Amplify Antitumor T-Cell Immunity. *Nano Lett* [Internet]. 2018 Jul 11;18(7):4377–85. Available from: <https://doi.org/10.1021/acs.nanolett.8b01406>
7. Sun W, Duan T, Cao Y, Li H. An Injectable Self-Healing Protein Hydrogel with Multiple Dissipation Modes and Tunable Dynamic Response. *Biomacromolecules* [Internet]. 2019 Nov 11;20(11):4199–207. Available from: <https://doi.org/10.1021/acs.biomac.9b01114>
8. Huerta-López C, Alegre-Cebollada J. Protein Hydrogels: The Swiss Army Knife for Enhanced Mechanical and Bioactive Properties of Biomaterials. *Nanomaterials* [Internet]. 2021;11(7). Available from: <https://www.mdpi.com/2079-4991/11/7/1656>
9. Lee KZ, Jeon J, Jiang B, Subramani SV, Li J, Zhang F. Protein-Based Hydrogels and Their Biomedical Applications. *Molecules* [Internet]. 2023;28(13). Available from: <https://www.mdpi.com/1420-3049/28/13/4988>



10. Draper ER, Adams DJ. How should multicomponent supramolecular gels be characterised? *Chem Soc Rev* [Internet]. 2018;47(10):3395–405. Available from: <http://dx.doi.org/10.1039/C7CS00804J> View Article Online
DOI: 10.1039/D4FD00204K
11. Yu G, Yan X, Han C, Huang F. Characterization of supramolecular gels. *Chem Soc Rev* [Internet]. 2013;42(16):6697–722. Available from: <http://dx.doi.org/10.1039/C3CS60080G>
12. MacDonald CRM, Draper ER. Applications of microscopy and small angle scattering techniques for the characterisation of supramolecular gels. *Beilstein Journal of Organic Chemistry* [Internet]. 2024;20:2608–34. Available from: <https://doi.org/10.3762/bjoc.20.220>
13. Raghuwanshi VS, Garnier G. Characterisation of hydrogels: Linking the nano to the microscale. *Adv Colloid Interface Sci* [Internet]. 2019;274:102044. Available from: <https://www.sciencedirect.com/science/article/pii/S0001868619302477>
14. McDowall D, Adams DJ, Seddon AM. Using small angle scattering to understand low molecular weight gels. *Soft Matter* [Internet]. 2022;18(8):1577–90. Available from: <http://dx.doi.org/10.1039/D1SM01707A>
15. Kubota R, Tanaka W, Hamachi I. Microscopic Imaging Techniques for Molecular Assemblies: Electron, Atomic Force, and Confocal Microscopies. *Chem Rev* [Internet]. 2021 Nov 24;121(22):14281–347. Available from: <https://doi.org/10.1021/acs.chemrev.0c01334>
16. Jayawardena I, Turunen P, Garms BC, Rowan A, Corrie S, Grøndahl L. Evaluation of techniques used for visualisation of hydrogel morphology and determination of pore size distributions. *Mater Adv* [Internet]. 2023;4(2):669–82. Available from: <http://dx.doi.org/10.1039/D2MA00932C>
17. Marmorat C, Arinstein A, Koifman N, Talmon Y, Zussman E, Rafailovich M. Cryo-Imaging of Hydrogels Supermolecular Structure. *Sci Rep* [Internet]. 2016;6(1):25495. Available from: <https://doi.org/10.1038/srep25495>
18. Wang L, Shi X, Wang J. A temperature-responsive supramolecular hydrogel: preparation, gel–gel transition and molecular aggregation. *Soft Matter* [Internet]. 2018;14(16):3090–5. Available from: <http://dx.doi.org/10.1039/C8SM00220G>
19. Boekhoven J, Poolman JM, Maity C, Li F, van der Mee L, Minkenberg CB, et al. Catalytic control over supramolecular gel formation. *Nat Chem* [Internet]. 2013;5(5):433–7. Available from: <https://doi.org/10.1038/nchem.1617>
20. Liu Q, Wang Y, Li W, Wu L. Structural Characterization and Chemical Response of a Ag-Coordinated Supramolecular Gel. *Langmuir* [Internet]. 2007 Jul 1;23(15):8217–23. Available from: <https://doi.org/10.1021/la700364t>
21. Kiyonaka S, Zhou SL, Hamachi I. pH-Responsive Phase Transition of Supramolecular Hydrogel Consisting of Glycosylated Amino Acetate and Carboxylic Acid Derivative. *Supramol Chem* [Internet]. 2003 Oct 1;15(7–8):521–8. Available from: <https://doi.org/10.1080/10610270310001605115>
22. Martinez-Garcia FD, Fischer T, Hayn A, Mierke CT, Burgess JK, Harmsen MC. A Beginner's Guide to the Characterization of Hydrogel Microarchitecture for Cellular Applications. *Gels* [Internet]. 2022;8(9). Available from: <https://www.mdpi.com/2310-2861/8/9/535>
23. Egerton RF, Zhu Y. Spatial resolution in secondary-electron microscopy. *Microscopy* [Internet]. 2023 Apr 1;72(2):66–77. Available from: <https://doi.org/10.1093/jmicro/dfac022>



24. Bray DF, Bagu J, Kogler P. Comparison of hexamethyldisilazane (HMDS), Peldri II, and critical-point drying methods for scanning electron microscopy of biological specimens. *Microsc Res Tech* [Internet]. 1993;26(6):489–95. Available from: <https://analyticalsciencejournals.onlinelibrary.wiley.com/doi/abs/10.1002/jemt.1070260603> DOI: 10.1039/D4FD000204K
25. Paterson SM, Casadio YS, Brown DH, Shaw JA, Chirila T V, Baker M V. Laser scanning confocal microscopy versus scanning electron microscopy for characterization of polymer morphology: Sample preparation drastically distorts morphologies of poly(2-hydroxyethyl methacrylate)-based hydrogels. *J Appl Polym Sci* [Internet]. 2013;127(6):4296–304. Available from: <https://onlinelibrary.wiley.com/doi/abs/10.1002/app.38034>
26. Merryweather DJ, Weston N, Roe J, Parmenter C, Lewis MP, Roach P. Exploring the microstructure of hydrated collagen hydrogels under scanning electron microscopy. *J Microsc* [Internet]. 2023;290(1):40–52. Available from: <https://onlinelibrary.wiley.com/doi/abs/10.1111/jmi.13174>
27. Koch M, Włodarczyk-Biegun MK. Faithful scanning electron microscopic (SEM) visualization of 3D printed alginate-based scaffolds. *Bioprinting* [Internet]. 2020;20:e00098. Available from: <https://www.sciencedirect.com/science/article/pii/S2405886620300257>
28. Efthymiou C, Williams MAK, McGrath KM. Revealing the structure of high-water content biopolymer networks: Diminishing freezing artefacts in cryo-SEM images. *Food Hydrocoll* [Internet]. 2017;73:203–12. Available from: <https://www.sciencedirect.com/science/article/pii/S0268005X16310219>
29. Fleck RA. Low-Temperature Electron Microscopy: Techniques and Protocols. In: Wolkers Willem F. and Oldenhof H, editor. *Cryopreservation and Freeze-Drying Protocols* [Internet]. New York, NY: Springer New York; 2015. p. 243–74. Available from: https://doi.org/10.1007/978-1-4939-2193-5_9
30. Serp D, Mueller M, von Stockar U, Marison IW. Low-temperature electron microscopy for the study of polysaccharide ultrastructures in hydrogels. I. Theoretical and technical considerations. *Biotechnol Bioeng* [Internet]. 2002;79(3):243–52. Available from: <https://analyticalsciencejournals.onlinelibrary.wiley.com/doi/abs/10.1002/bit.10286>
31. Bachmann L, Mayer E. Physics of Water and Ice: Implications for Cryofixation. In: Steinbrecht RA, Zierold K, editors. *Cryotechniques in Biological Electron Microscopy* [Internet]. Berlin, Heidelberg: Springer Berlin Heidelberg; 1987. p. 3–34. Available from: https://doi.org/10.1007/978-3-642-72815-0_1
32. Dubochet J. The Physics of Rapid Cooling and Its Implications for Cryoimmobilization of Cells. In: *Cellular Electron Microscopy* [Internet]. Academic Press; 2007. p. 7–21. (Methods in Cell Biology; vol. 79). Available from: <https://www.sciencedirect.com/science/article/pii/S0091679X0679001X>
33. Hurbain I, Sachse M. The future is cold: cryo-preparation methods for transmission electron microscopy of cells. *Biol Cell* [Internet]. 2011 Sep 1;103(9):405–20. Available from: <https://doi.org/10.1042/BC20110015>
34. Dubochet J, Stahlberg H. Electron Cryomicroscopy. In: *eLS* [Internet]. John Wiley & Sons, Ltd; 2001. Available from: <https://onlinelibrary.wiley.com/doi/abs/10.1038/npg.els.0002999>
35. Shimoni, Müller. On optimizing high-pressure freezing: from heat transfer theory to a new microbioscopy device. *J Microsc* [Internet]. 1998 Dec 1;192(3):236–47. Available from: <https://doi.org/10.1046/j.1365-2818.1998.00389.x>



36. Weissenberger G, Henderikx RJM, Peters PJ. Understanding the invisible hands of sample preparation for cryo-EM. *Nat Methods* [Internet]. 2021;18(5):463–71. Available from: <https://doi.org/10.1038/s41592-021-01130-6> View Article Online
DOI: 10.1039/D4FD00204K
37. Khoury LR, Popa I. Chemical unfolding of protein domains induces shape change in programmed protein hydrogels. *Nat Commun* [Internet]. 2019;10(1):5439. Available from: <https://doi.org/10.1038/s41467-019-13312-0>
38. Lantigua D, Nguyen MA, Wu X, Suvarnapathaki S, Kwon S, Gavin W, et al. Synthesis and characterization of photocrosslinkable albumin-based hydrogels for biomedical applications. *Soft Matter* [Internet]. 2020;16(40):9242–52. Available from: <http://dx.doi.org/10.1039/D0SM00977F>
39. Ma X, Sun X, Hargrove D, Chen J, Song D, Dong Q, et al. A Biocompatible and Biodegradable Protein Hydrogel with Green and Red Autofluorescence: Preparation, Characterization and In Vivo Biodegradation Tracking and Modeling. *Sci Rep* [Internet]. 2016;6(1):19370. Available from: <https://doi.org/10.1038/srep19370>
40. Fang J, Mehlich A, Koga N, Huang J, Koga R, Gao X, et al. Forced protein unfolding leads to highly elastic and tough protein hydrogels. *Nat Commun* [Internet]. 2013;4(1):2974. Available from: <https://doi.org/10.1038/ncomms3974>
41. Lopez Mora N, Owens M, Schmidt S, Silva AF, Bradley M. Poly-Epsilon-Lysine Hydrogels with Dynamic Crosslinking Facilitates Cell Proliferation. *Materials* [Internet]. 2020;13(17). Available from: <https://www.mdpi.com/1996-1944/13/17/3851>
42. Kyomugasho C, Christiaens S, Van de Walle D, Van Loey AM, Dewettinck K, Hendrickx ME. Evaluation of cation-facilitated pectin-gel properties: Cryo-SEM visualisation and rheological properties. *Food Hydrocoll* [Internet]. 2016;61:172–82. Available from: <https://www.sciencedirect.com/science/article/pii/S0268005X16302156>
43. Kim JY, Song JY, Lee EJ, Park SK. Rheological properties and microstructures of Carbopol gel network system. *Colloid Polym Sci* [Internet]. 2003;281(7):614–23. Available from: <https://doi.org/10.1007/s00396-002-0808-7>
44. Yu X, Cai J, Xu M, Li Q, Yang Y, Wan Z, et al. A natural food-grade supramolecular self-assembly system for creation of hierarchically structured hydrogels. *Nanoscale* [Internet]. 2024;16(30):14261–8. Available from: <http://dx.doi.org/10.1039/D4NR01410C>
45. Sosinsky GE, Crum J, Jones YZ, Lanman J, Smarr B, Terada M, et al. The combination of chemical fixation procedures with high pressure freezing and freeze substitution preserves highly labile tissue ultrastructure for electron tomography applications. *J Struct Biol* [Internet]. 2008;161(3):359–71. Available from: <https://www.sciencedirect.com/science/article/pii/S1047847707002201>
46. Dahl R, Staehelin LA. High-pressure freezing for the preservation of biological structure: Theory and practice. *J Electron Microscop Tech* [Internet]. 1989 Nov 1;13(3):165–74. Available from: <https://doi.org/10.1002/jemt.1060130305>
47. Studer D, Humbel BM, Chiquet M. Electron microscopy of high pressure frozen samples: bridging the gap between cellular ultrastructure and atomic resolution. *Histochem Cell Biol* [Internet]. 2008;130(5):877–89. Available from: <https://doi.org/10.1007/s00418-008-0500-1>
48. Sosinsky GE, Crum J, Jones YZ, Lanman J, Smarr B, Terada M, et al. The combination of chemical fixation procedures with high pressure freezing and freeze substitution preserves highly labile tissue ultrastructure for electron tomography applications. *J Struct Biol* [Internet].



- 2008;161(3):359–71. Available from: <https://www.sciencedirect.com/science/article/pii/S1047847707002201> View Article Online
DOI: 10.1039/D4FD00204K
49. Sartori N, Richter K, Dubochet J. Vitrification depth can be increased more than 10-fold by high-pressure freezing. *J Microsc* [Internet]. 1993 Oct 1;172(1):55–61. Available from: <https://doi.org/10.1111/j.1365-2818.1993.tb03393.x>
50. Aston R, Sewell K, Klein T, Lawrie G, Grøndahl L. Evaluation of the impact of freezing preparation techniques on the characterisation of alginate hydrogels by cryo-SEM. *Eur Polym J* [Internet]. 2016;82:1–15. Available from: <https://www.sciencedirect.com/science/article/pii/S001430571630653X>
51. Navarra G, Peres C, Contardi M, Picone P, San Biagio PL, Di Carlo M, et al. Heat- and pH-induced BSA conformational changes, hydrogel formation and application as 3D cell scaffold. *Arch Biochem Biophys* [Internet]. 2016;606:134–42. Available from: <https://www.sciencedirect.com/science/article/pii/S0003986116302703>
52. Khanna S, Singh AK, Behera SP, Gupta S. Thermoresponsive BSA hydrogels with phase tunability. *Materials Science and Engineering: C* [Internet]. 2021;119:111590. Available from: <https://www.sciencedirect.com/science/article/pii/S0928493120335086>
53. Nicolai T, Chassenieux C. Heat-induced gelation of plant globulins. *Curr Opin Food Sci* [Internet]. 2019;27:18–22. Available from: <https://www.sciencedirect.com/science/article/pii/S2214799318300833>
54. Ren W, Xia W, Gunes DZ, Ahrné L. Heat-induced gels from pea protein soluble colloidal aggregates: Effect of calcium addition or pH adjustment on gelation behavior and rheological properties. *Food Hydrocoll* [Internet]. 2024;147:109417. Available from: <https://www.sciencedirect.com/science/article/pii/S0268005X23009633>
55. Lv S, Dudek DM, Cao Y, Balamurali MM, Gosline J, Li H. Designed biomaterials to mimic the mechanical properties of muscles. *Nature* [Internet]. 2010;465(7294):69–73. Available from: <https://doi.org/10.1038/nature09024>
56. Li Y, Xue B, Cao Y. 100th Anniversary of Macromolecular Science Viewpoint: Synthetic Protein Hydrogels. *ACS Macro Lett* [Internet]. 2020 Apr 21;9(4):512–24. Available from: <https://doi.org/10.1021/acsmacrolett.0c00109>
57. Li H, Kong N, Laver B, Liu J. Hydrogels Constructed from Engineered Proteins. *Small* [Internet]. 2016 Feb 1;12(8):973–87. Available from: <https://doi.org/10.1002/sml.201502429>
58. Wei K, Senturk B, Matter MT, Wu X, Herrmann IK, Rottmar M, et al. Mussel-Inspired Injectable Hydrogel Adhesive Formed under Mild Conditions Features Near-Native Tissue Properties. *ACS Appl Mater Interfaces* [Internet]. 2019 Dec 26;11(51):47707–19. Available from: <https://doi.org/10.1021/acsmi.9b16465>
59. Kong N, Fu L, Peng Q, Li H. Metal Chelation Dynamically Regulates the Mechanical Properties of Engineered Protein Hydrogels. *ACS Biomater Sci Eng* [Internet]. 2017 May 8;3(5):742–9. Available from: <https://doi.org/10.1021/acsbomaterials.6b00374>
60. Zhou ML, Qian ZG, Chen L, Kaplan DL, Xia XX. Rationally Designed Redox-Sensitive Protein Hydrogels with Tunable Mechanical Properties. *Biomacromolecules* [Internet]. 2016 Nov 14;17(11):3508–15. Available from: <https://doi.org/10.1021/acs.biomac.6b00973>
61. Duan T, Li H. In Situ Phase Transition of Elastin-Like Polypeptide Chains Regulates Thermoresponsive Properties of Elastomeric Protein-Based Hydrogels. *Biomacromolecules*



- [Internet]. 2020 Jun 8;21(6):2258–67. Available from: <https://doi.org/10.1021/acs.biomac.0c00206>
- View Article Online
DOI: 10.1039/D4FD00204K
62. Fu L, Haage A, Kong N, Tanentzapf G, Li H. Dynamic protein hydrogels with reversibly tunable stiffness regulate human lung fibroblast spreading reversibly. *Chem Commun* [Internet]. 2019;55(36):5235–8. Available from: <http://dx.doi.org/10.1039/C9CC01276A>
63. Kong N, Peng Q, Li H. Rationally Designed Dynamic Protein Hydrogels with Reversibly Tunable Mechanical Properties. *Adv Funct Mater* [Internet]. 2014 Dec 1;24(46):7310–7. Available from: <https://doi.org/10.1002/adfm.201402205>
64. Khoury LR, Slawinski M, Collison DR, Popa I. Cation-induced shape programming and morphing in protein-based hydrogels. *Sci Adv* [Internet]. 2020;6(18):eaba6112. Available from: <https://www.science.org/doi/abs/10.1126/sciadv.aba6112>
65. Wu J, Li P, Dong C, Jiang H, Xue B, Gao X, et al. Rationally designed synthetic protein hydrogels with predictable mechanical properties. *Nat Commun* [Internet]. 2018;9(1):620. Available from: <https://doi.org/10.1038/s41467-018-02917-6>
66. Knoff DS, Szczublewski H, Altamirano D, Fajardo Cortes KA, Kim M. Cytoskeleton-Inspired Artificial Protein Design to Enhance Polymer Network Elasticity. *Macromolecules* [Internet]. 2020 May 12;53(9):3464–71. Available from: <https://doi.org/10.1021/acs.macromol.0c00514>
67. Dranseike D, Ota Y, Edwardson TGW, Guzzi EA, Hori M, Nakic ZR, et al. Designed modular protein hydrogels for biofabrication. *Acta Biomater* [Internet]. 2024;177:107–17. Available from: <https://www.sciencedirect.com/science/article/pii/S1742706124000886>
68. Hughes MDG, Cussons S, Hanson BS, Cook KR, Feller T, Mahmoudi N, et al. Building block aspect ratio controls assembly, architecture, and mechanics of synthetic and natural protein networks. *Nat Commun* [Internet]. 2023;14(1):5593. Available from: <https://doi.org/10.1038/s41467-023-40921-7>
69. da Silva MA, Lenton S, Hughes M, Brockwell DJ, Dougan L. Assessing the Potential of Folded Globular Polyproteins As Hydrogel Building Blocks. *Biomacromolecules* [Internet]. 2017 Feb 13;18(2):636–46. Available from: <https://doi.org/10.1021/acs.biomac.6b01877>
70. Hughes MDG, Hanson BS, Cussons S, Mahmoudi N, Brockwell DJ, Dougan L. Control of Nanoscale In Situ Protein Unfolding Defines Network Architecture and Mechanics of Protein Hydrogels. *ACS Nano* [Internet]. 2021;15(7):11296–308. Available from: <https://doi.org/10.1021/acsnano.1c00353>
71. Sadaba N, Sanchez-Rexach E, Waltmann C, Hilburg SL, Pozzo LD, Olvera de la Cruz M, et al. Strain learning in protein-based mechanical metamaterials. *Proceedings of the National Academy of Sciences* [Internet]. 2024 Nov 5;121(45):e2407929121. Available from: <https://doi.org/10.1073/pnas.2407929121>
72. Fu L, Li L, Bian Q, Xue B, Jin J, Li J, et al. Cartilage-like protein hydrogels engineered via entanglement. *Nature* [Internet]. 2023;618(7966):740–7. Available from: <https://doi.org/10.1038/s41586-023-06037-0>
73. Hughes MDG, Cussons S, Mahmoudi N, Brockwell DJ, Dougan L. Tuning Protein Hydrogel Mechanics through Modulation of Nanoscale Unfolding and Entanglement in Postgelation Relaxation. *ACS Nano* [Internet]. 2022 Jul 26;16(7):10667–78. Available from: <https://doi.org/10.1021/acsnano.2c02369>



74. Kong F, Mehwish N, Lee BH. Emerging albumin hydrogels as personalized biomaterials. *Acta Biomater* [Internet]. 2023;157:67–90. Available from: <https://www.sciencedirect.com/science/article/pii/S1742706122007930> DOI: 10.1039/D4FD00204K
75. Meng R, Zhu H, Deng P, Li M, Ji Q, He H, et al. Research progress on albumin-based hydrogels: Properties, preparation methods, types and its application for antitumor-drug delivery and tissue engineering. *Front Bioeng Biotechnol* [Internet]. 2023;11. Available from: <https://www.frontiersin.org/journals/bioengineering-and-biotechnology/articles/10.3389/fbioe.2023.1137145>
76. Xu X, Hu J, Xue H, Hu Y, Liu Y nan, Lin G, et al. Applications of human and bovine serum albumins in biomedical engineering: A review. *Int J Biol Macromol* [Internet]. 2023;253:126914. Available from: <https://www.sciencedirect.com/science/article/pii/S0141813023038114>
77. Wiita AP, Ainavarapu SRK, Huang HH, Fernandez JM. Force-dependent chemical kinetics of disulfide bond reduction observed with single-molecule techniques. *Proceedings of the National Academy of Sciences* [Internet]. 2006;103(19):7222–7. Available from: <https://www.pnas.org/doi/abs/10.1073/pnas.0511035103>
78. Grandbois M, Beyer M, Rief M, Clausen-Schaumann H, Gaub HE. How Strong Is a Covalent Bond? *Science* (1979) [Internet]. 1999;283(5408):1727–30. Available from: <https://www.science.org/doi/abs/10.1126/science.283.5408.1727>
79. Hughes MDG, Cussons S, Mahmoudi N, Brockwell DJ, Dougan L. Single molecule protein stabilisation translates to macromolecular mechanics of a protein network. *Soft Matter* [Internet]. 2020;16(27):6389–99. Available from: <http://dx.doi.org/10.1039/C9SM02484K>
80. Fancy DA, Kodadek T. Chemistry for the analysis of protein–protein interactions: Rapid and efficient cross-linking triggered by long wavelength light. *Proceedings of the National Academy of Sciences* [Internet]. 1999;96(11):6020–4. Available from: <https://www.pnas.org/doi/abs/10.1073/pnas.96.11.6020>
81. Brown CP, Hughes MDG, Mahmoudi N, Brockwell DJ, Coletta PL, Peyman S, et al. Structural and mechanical properties of folded protein hydrogels with embedded microbubbles. *Biomater Sci* [Internet]. 2023;11(8):2726–37. Available from: <http://dx.doi.org/10.1039/D2BM01918C>
82. Hughes MDG, Cook KR, Cussons S, Boroumand A, Tyler All, Head D, et al. Capturing Dynamic Assembly of Nanoscale Proteins During Network Formation. *Small* [Internet]. 2024 Nov 12;2407090. Available from: <https://doi.org/10.1002/sml.202407090>
83. Hughes MDG, West D, Wurr R, Cussons S, Cook KR, Mahmoudi N, et al. Competition between cross-linking and force-induced local conformational changes determines the structure and mechanics of labile protein networks. *J Colloid Interface Sci* [Internet]. 2025;678:1259–69. Available from: <https://www.sciencedirect.com/science/article/pii/S0021979724022483>
84. Schindelin J, Arganda-Carreras I, Frise E, Kaynig V, Longair M, Pietzsch T, et al. Fiji: an open-source platform for biological-image analysis. *Nat Methods* [Internet]. 2012;9(7):676–82. Available from: <https://doi.org/10.1038/nmeth.2019>
85. Teixeira J. Small-angle scattering by fractal systems. *J Appl Crystallogr* [Internet]. 1988 Dec;21(6):781–5. Available from: <https://doi.org/10.1107/S0021889888000263>
86. Liu R, Cai Z, Zhang Q, Yuan H, Zhang G, Yang D. Colorimetric two-dimensional photonic crystal biosensors for label-free detection of hydrogen peroxide. *Sens Actuators B Chem* [Internet]. 2022;354:131236. Available from: <https://www.sciencedirect.com/science/article/pii/S0925400521018049>



87. Zhang X, Jiang S, Yan T, Fan X, Li F, Yang X, et al. Injectable and fast self-healing protein hydrogels. *Soft Matter* [Internet]. 2019;15(38):7583–9. Available from: <http://dx.doi.org/10.1039/C9SM01543D> View Article Online
DOI: 10.1039/D4FD00204K
88. Knoll G, Verkleij AJ, Plattner H. Cryofixation of Dynamic Processes in Cells and Organelles. In: Steinbrecht RA, Zierold K, editors. *Cryotechniques in Biological Electron Microscopy* [Internet]. Berlin, Heidelberg: Springer Berlin Heidelberg; 1987. p. 258–71. Available from: https://doi.org/10.1007/978-3-642-72815-0_14
89. Ivan'kova EM, Dobrovolskaya IP, Popryadukhin P V, Kryukov A, Yudin VE, Morganti P. In-situ cryo-SEM investigation of porous structure formation of chitosan sponges. *Polym Test* [Internet]. 2016;52:41–5. Available from: <https://www.sciencedirect.com/science/article/pii/S0142941815301677>
90. Buchheim W. Aspects of Sample Preparation for Freeze-Fracture/Freeze-Etch Studies of Proteins and Lipids in Food Systems: A Review. *Food Structure*. 1982;1(2).
91. Annabi N, Nichol JW, Zhong X, Ji C, Koshy S, Khademhosseini A, et al. Controlling the Porosity and Microarchitecture of Hydrogels for Tissue Engineering. *Tissue Eng Part B Rev* [Internet]. 2010;16(4):371–83. Available from: <https://doi.org/10.1089/ten.teb.2009.0639>
92. Kang HW, Tabata Y, Ikada Y. Fabrication of porous gelatin scaffolds for tissue engineering. *Biomaterials* [Internet]. 1999;20(14):1339–44. Available from: <https://www.sciencedirect.com/science/article/pii/S0142961299000368>
93. Madhally S V, Matthew HWT. Porous chitosan scaffolds for tissue engineering. *Biomaterials* [Internet]. 1999;20(12):1133–42. Available from: <https://www.sciencedirect.com/science/article/pii/S0142961299000113>
94. Genevro GM, de Moraes MA, Beppu MM. Freezing influence on physical properties of glucomannan hydrogels. *Int J Biol Macromol* [Internet]. 2019;128:401–5. Available from: <https://www.sciencedirect.com/science/article/pii/S014181301835298X>
95. Loh QL, Choong C. Three-Dimensional Scaffolds for Tissue Engineering Applications: Role of Porosity and Pore Size. *Tissue Eng Part B Rev* [Internet]. 2013;19(6):485–502. Available from: <https://doi.org/10.1089/ten.teb.2012.0437>
96. Wu X, Black L, Santacana-Laffitte G, Patrick Jr. CW. Preparation and assessment of glutaraldehyde-crosslinked collagen–chitosan hydrogels for adipose tissue engineering. *J Biomed Mater Res A* [Internet]. 2007;81A(1):59–65. Available from: <https://onlinelibrary.wiley.com/doi/abs/10.1002/jbm.a.31003>
97. Aranaz I, Gutiérrez MC, Ferrer ML, Del Monte F. Preparation of Chitosan Nanocomposites with a Macroporous Structure by Unidirectional Freezing and Subsequent Freeze-Drying. *Mar Drugs* [Internet]. 2014;12(11):5619–42. Available from: <https://www.mdpi.com/1660-3397/12/11/5619>
98. Hondow N, Harrington J, Brydson R, Doak SH, Singh N, Manshian B, et al. STEM mode in the SEM: A practical tool for nanotoxicology. *Nanotoxicology* [Internet]. 2011 Jun 1;5(2):215–27. Available from: <https://doi.org/10.3109/17435390.2010.535622>
99. McIntosh JR. *Cellular electron microscopy*. Amsterdam ; Elsevier Academic Press; 2007. (Methods in cell biology, v. 79).
100. Belcher HA, Guthold M, Hudson NE. What is the diameter of a fibrin fiber? *Res Pract Thromb Haemost* [Internet]. 2023 Jul 1;7(5). Available from: <https://doi.org/10.1016/j.rpth.2023.100285>



101. Khater IM, Nabi IR, Hamarneh G. A Review of Super-Resolution Single-Molecule Localization Microscopy Cluster Analysis and Quantification Methods. *Patterns* [Internet]. 2020 Jun 12;1(3): Available from: <https://doi.org/10.1016/j.patter.2020.100038> DOI: 10.1039/D4FD00204K
102. de Vries JJ, Laan DM, Frey F, Koenderink GH, de Maat MPM. A systematic review and comparison of automated tools for quantification of fibrous networks. *Acta Biomater* [Internet]. 2023;157:263–74. Available from: <https://www.sciencedirect.com/science/article/pii/S1742706122008121>
103. Molteni M, Magatti D, Cardinali B, Rocco M, Ferri F. Fast Two-Dimensional Bubble Analysis of Biopolymer Filamentous Networks Pore Size from Confocal Microscopy Thin Data Stacks. *Biophys J* [Internet]. 2013 Mar 5;104(5):1160–9. Available from: <https://doi.org/10.1016/j.bpj.2013.01.016>
104. Münster S, Fabry B. A Simplified Implementation of the Bubble Analysis of Biopolymer Network Pores. *Biophys J* [Internet]. 2013 Jun 18;104(12):2774–5. Available from: <https://doi.org/10.1016/j.bpj.2013.05.016>
105. Eyisoğlu H, Hazekamp ED, Cruys J, Koenderink GH, de Maat MPM. Flow affects the structural and mechanical properties of the fibrin network in plasma clots. *J Mater Sci Mater Med* [Internet]. 2024;35(1):8. Available from: <https://doi.org/10.1007/s10856-024-06775-1>
106. Rossboth B, Arnold AM, Ta H, Platzer R, Kellner F, Huppa JB, et al. TCRs are randomly distributed on the plasma membrane of resting antigen-experienced T cells. *Nat Immunol* [Internet]. 2018;19(8):821–7. Available from: <https://doi.org/10.1038/s41590-018-0162-7>
107. Nevskiy O, Wöll D. 3D Super-Resolution Fluorescence Imaging of Microgels. *Annu Rev Phys Chem* [Internet]. 2023;74(Volume 74, 2023):391–414. Available from: <https://www.annualreviews.org/content/journals/10.1146/annurev-physchem-062422-022601>
108. Pedersen MC, Mukherjee S, Doostmohammadi A, Mondal C, Thijssen K. Active Particles Knead Three-Dimensional Gels into Porous Structures. *Phys Rev Lett* [Internet]. 2024 Nov 26;133(22):228301. Available from: <https://link.aps.org/doi/10.1103/PhysRevLett.133.228301>
109. Richtering W, Saunders BR. Gel architectures and their complexity. *Soft Matter* [Internet]. 2014;10(21):3695–702. Available from: <http://dx.doi.org/10.1039/C4SM00208C>



Data availability

All data will be available at the final proof stage.

[View Article Online](#)
DOI: 10.1039/D4FD00204K

